# SPECT Imaging using Pinhole Collimation

## System Design and Simulation Studies for Pre-Clinical and Clinical Imaging

Peterson, Mikael

2017

# SPECT Imaging using Pinhole Collimation

## System Design and Simulation Studies for Pre-Clinical and Clinical Imaging

MIKAEL PETERSON
FACULTY OF SCIENCE | LUND UNIVERSITY

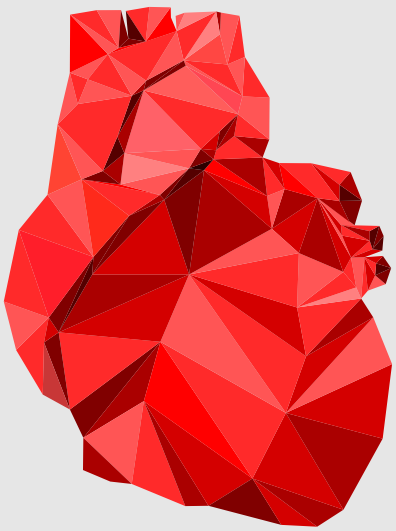

# SPECT Imaging using Pinhole Collimation

## System Design and Simulation Studies for Pre-Clinical and Clinical Imaging

Mikael Peterson

LUND
UNIVERSITY

DOCTORAL DISSERTATION
by due permission of the Faculty of Science,
Lund University, Sweden.
To be defended at Lecture Hall F3 at Skånes University Hospital, Lund
on 2017-09-22 at 9:00.

*Faculty opponent*
Hugo de Jong, PhD
Associate Professor at Utrecht University
Department of Radiology, Utrecht, Holland.

Organization: **LUND UNIVERSITY**
Department of Medical Radiation Physics
Skåne University Hospital, Lund
SE-221 85 LUND
Sweden

Author(s): Mikael Peterson

Document name: DOCTORAL DISSERTATION

Date of issue 2017-09-22

Sponsoring organization

Title and subtitle: SPECT Imaging using Pinhole Collimation - System Design and Simulation Studies for Pre-Clinical and Clinical Imaging

Abstract

The focus of this dissertation is the use of pinhole collimation in Nuclear Medicine. A pinhole is a single aperture in an opaque material that is placed between the detector and source of interest, and photons must pass through the hole to reach the detector. The choices of pinhole parameters, e.g. the pinhole material and size of the opening, are closely linked to the performance of the detector system.

Pinhole-based single-photon emission computed tomography (SPECT) has primarily been used to investigate human diseases in small animals because of the superior resolution and efficiency achieved with this type of collimation. The SPECT methodology involves determination of the radiopharmaceutical distribution within an object. An essential step in this methodology is the image reconstruction, i.e., the transformation of the acquired two-dimensional (2D) data into a three-dimensional (3D) distribution.

This dissertation describes the development of a SPECT system for small animal imaging called InSPECT. In Paper I, determination of the reconstructed resolution for a prototype setup with a video-based detector system is discussed, and in Paper II, construction of the InSPECT system with eight separate video detectors is described. A fusible metal, Rose's metal, was used to cast the centre bore, in which platinum pinholes were mounted. The cast pieces could adequately shield the detectors and could be machined with a high precision. Thus, Rose's metal, which is relatively inexpensive, could be employed for pinhole collimation but would lead to image characteristics that are less favourable than those achievable using gold or platinum pinholes. In Paper III, we present an evaluation of the performance of Rose's metal pinholes and a comparison with other pinhole materials.

Monte Carlo-based computer models can be utilised to simulate the image formation process and can enable expensive and time-consuming instrumentation changes to be evaluated prior to building prototypes. In Paper IV, we discuss the implementation of a cadmium zinc telluride (CZT) semiconductor detector model in the Monte Carlo program SIMIND. The accuracy of the model was confirmed by comparing its results to measurements. In Paper V, we address the use of the CZT model in an SIMIND-based maximum-likelihood–expectation-maximisation iterative reconstruction of the measured data. The images reconstructed using the computer model enabled the quantification of the total activity without requiring calibration of the detector count per unit second per unit activity. In Paper VI, we describe the simulation of a dedicated SPECT scanner that employs 19 semiconductor detector–pinhole units for myocardial perfusion imaging. Compared to conventional SPECT devices, this camera is more efficient, and the efficiency is often traded for a reduction in imaging times and patient doses. An alternative use of the efficiency is to use smaller pinhole which yields better spatial resolution in the projections. No increase in contrast-to-noise was seen for smaller pinholes since any increase in contrast was also accompanied by an equal increase in noise. Also, changes in transmurality affected the CNR to a greater extent than did changes in lesion extent.

Key words: Pinhole SPECT tomography, Nuclear medicine imaging, Monte Carlo-based image reconstruction

Classification system and/or index terms (if any)

Supplementary bibliographical information — Language: English

ISSN and key title — ISBN: 978-91-7753-377-1 (print)
978-91-7753-378-8 (pdf)

Recipient's notes — Number of pages 167 — Price

Security classification



Signature 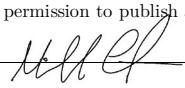 Date 2017-08-14

# SPECT Imaging using Pinhole Collimation

## System Design and Simulation Studies for Pre-Clinical and Clinical Imaging

Mikael Peterson


LUND
UNIVERSITY

Faculty of Science
Department of Medical Radiation Physics

978-91-7753-377-1 (print)
978-91-7753-378-8 (pdf)

Printed in Sweden by Media-Tryck, Lund University
Lund 2017

Between my finger and my thumb
The squat pen rests; snug as a gun.

My grandfather cut more turf in a day
Than any other man on Toner's bog.
Once I carried him milk in a bottle
Corked sloppily with paper. He straightened up
To drink it, then fell to right away
Nicking and slicing neatly, heaving sods
Over his shoulder, going down and down
For the good turf. Digging.

The cold smell of potato mould, the squelch and slap
Of soggy peat, the curt cuts of an edge
Through living roots awaken in my head.
But I've no spade to follow men like them.

Between my finger and my thumb
The squat pen rests.
I'll dig with it.

**Seamus Heaney's poem 'Digging'**

# Contents

# Abbreviations

| | |
|---|---|
| 2D: | Two-dimensional |
| 3D: | Three-dimensional |
| CNR: | Contrast-to-noise ratio |
| CCD: | Charge-coupled device |
| CsI(Tl): | Caesium-iodine crystal doped with thallium |
| CT: | Computed tomography |
| CZT: | Cadmium zinc telluride |
| DOI: | Depth of interaction |
| FOV: | Field of view |
| NaI(Tl): | Sodium-iodine crystal doped with thallium |
| SPECT: | Single-photon emission computed tomography |
| PDF: | Probability density function |
| PET: | Positron emission tomography |
| PMT: | Photomultiplier tube |
| PVE: | Partial-volume effect |
| QE: | Quantum efficiency |

# Populärvetenskaplig sammanfattning

Nuklearmedicinsk bildtagning med hjälp av radiofarmaka är ett viktigt verktyg för att studera biologiska processer och humansjukdomar. Bildtagning sker ofta med en detektor i kombination med en kollimator. En typ av kollimering är pinnhålskollimering, där ett pinnhål i ett opakt material placeras mellan en källa och en detektor. Pinnhålet fyller samma funktion som en optisk lins då emitterade fotoner måste passera genom hålet för att nå detektorn. Valet av pinnhålsparametrar, exempelvis material och storlek på öppningen, spelar stor roll för detektorsystemets slutgiltiga prestanda.

Pinnhålskollimering används även vid Single-photon emission computed tomography (SPECT). Denna metodik avser både bildtagning från flera vinklar och rekonstruktion av radiofarmakats tredimensionella fördelning. Pinnhålsbaserad SPECT används bland annat för att studera humansjukdomar i djurmodeller, så som råttor och möss. För detta är pinnhålskollimering ett utmärkt val då tekniken tillåter förstoring av små strukturer och därför kan avbilda aktivitetsfördelningar med hög upplösning.

I denna avhandling beskrivs utvecklingen av ett tomografiskt smådjurskamerasystem vid namn InSPECT. Artikel I beskriver mätningar och bestämningen av den rekonstruerade upplösningen för en prototypuppställning bestående av en videodetektor i kombination med ett pinnhål. I artikel II beskrivs byggandet av ett kamerasystem med åtta videodetektorer (ett pinnhål per detektor). Vi använde Roses metall för att tillverka ett centralstycke som både skärmar detektorerna och tillät montering av platinapinnhål. Fördelen med Roses metall är att den har hög densitet och atomnummer, låg smältpunkt och att de gjutna delarna kan bearbetas med hög precision. Materialet kan även användas för pinnhålskollimering. Fördelen är att Roses metall är billigt jämfört med exempelvis pinnhål av guld och platina, men bildkvalitén påverkas negativt av att en högre andel fotoner penetrerar och sprids i pinnhålsmaterialet. I artikel III presenteras en utvärdering av bildprestandan för pinnhål av Roses metall och en jämförelse med andra pinnhålsmaterial.

Ett sätt att simulera bildtagning med pinnhål är att använda Monte Carlo-program. Dessa program simulerar fotontransport och detektion för en given mätgeometri och detektor. Med Monte Carlo-simuleringar går det exempelvis att utvärdera dyra och tidskrävande förändringar i hårdvara istället för att bygga prototyper. Artikel IV avhandlar implementeringen av en halvledardetektormodell, baserad på halvledarmaterialet CZT, i Monte Carlo-programmet SIMIND. Modellens goda noggrannhet bekräftades genom jämförelser med mätt data. I artikel V används CZT-modellen för Monte Carlo-baserad rekonstruktion av data från ett kliniskt SPECT-system. De rekonstruerade bilderna är kvantitativa och behöver ej normeras med hjälp av en extern kalibrering. Artikel VI beskriver simuleringen av en dedikerad SPECT-kamera med 19 detektor-pinnhålenheter som används vid myokardscintigrafi. De dedikerade pinnhålssystemen har högre känslighet än konventionella system, vilket används för att korta undersökningstider och minska patientdoser. Ett annat alternativ, som också minskar känsligheten, är att minska storleken på pinnhålet vilket leder till bättre upplösning. Våra resultat visar att kontrast-till-brus-förhållandet inte gynnas av mindre pinnhål.

# Abstract

The focus of this dissertation is the use of pinhole collimation in Nuclear Medicine. A pinhole is a single aperture in an opaque material that is placed between the detector and source of interest, and photons must pass through the hole to reach the detector. The choices of pinhole parameters, e.g. the pinhole material and size of the opening, are closely linked to the performance of the detector system.

Pinhole-based single-photon emission computed tomography (SPECT) has primarily been used to investigate human diseases in small animals because of the superior resolution and efficiency achieved with this type of collimation. The SPECT methodology involves determination of the radiopharmaceutical distribution within an object. An essential step in this methodology is the image reconstruction, i.e., the transformation of the acquired two-dimensional (2D) data into a three-dimensional (3D) distribution.

This dissertation describes the development of a SPECT system for small animal imaging called InSPECT. In Paper I, determination of the reconstructed resolution for a prototype setup with a video-based detector system is discussed, and in Paper II, construction of the InSPECT system with eight separate video detectors is described. A fusible metal, Rose's metal, was used to cast the centre bore, in which platinum pinholes were mounted. The cast pieces could adequately shield the detectors and could be machined with a high precision. Thus, Rose's metal, which is relatively inexpensive, could be employed for pinhole collimation but would lead to image characteristics that are less favourable than those achievable using gold or platinum pinholes. In Paper III, we present an evaluation of the performance of Rose's metal pinholes and a comparison with other pinhole materials.

Monte Carlo-based computer models can be utilised to simulate the image formation process and can enable expensive and time-consuming instrumentation changes to be evaluated prior to building prototypes. In Paper IV, we discuss the implementation of a cadmium zinc telluride (CZT) semiconductor detector model in the Monte Carlo program SIMIND. The

accuracy of the model was confirmed by comparing its results to measurements. In Paper V, we address the use of the CZT model in an SIMIND-based maximum-likelihood–expectation-maximisation iterative reconstruction of the measured data. The images reconstructed using the computer model enabled the quantification of the total activity without requiring calibration of the detector count per second per unit activity. In Paper VI, we describe the simulation of a dedicated SPECT scanner that employs 19 semiconductor detector–pinhole units for myocardial perfusion imaging. Compared to conventional SPECT devices, this camera is more efficient, and the efficiency is often traded for a reduction in imaging times and patient doses. An alternative use of the efficiency is to use smaller pinhole which yields better spatial resolution in the projections. No increase in contrast-to-noise was seen for smaller pinholes since any increase in contrast was also accompanied by an equal increase in noise. Also, changes in transmurality affected the CNR to a greater extent than did changes in lesion extent.

# List of Original Papers

I. **Construction of a pre-clinical high resolution tomographic scintillation camera system**
Mikael Peterson, Kaj Ljunggren, John Palmer, and Sven-Erik Strand
*IEEE Nuclear Science Symposium & Medical Imaging Conference Record*, 2009, pp. 3670-3671.

II. **A method for using high density fusible Rose's metal with high precision machining in small animal imaging applications**
Mikael Peterson, Kaj Ljunggren, Lars Andersson-Ljus, Brian Miller, and Sven-Erik Strand
*IEEE Nuclear Science Symposium & Medical Imaging Conference Record*, 2010, pp. 3155-3157.

III. **Using Rose's metal alloy as a pinhole collimator material in preclinical small-animal imaging: a Monte Carlo evaluation**
Mikael Peterson, Sven-Erik Strand, and Michael Ljungberg
*Medical Physics*, 2015, vol. 42, pp. 1698-709.

IV. **Monte Carlo simulations of the GE Discovery Alcyone CZT SPECT systems**
Hendrik Pretorius, Chi Liu, Peng Fan, Mikael Peterson, and Michael Ljungberg
*IEEE Transactions on Nuclear Science*, 2015, vol. 62, pp. 832-839.

**V.** **Monte Carlo-Based quantitative pinhole SPECT reconstruction using a ray-tracing back-projector**
Mikael Peterson, Johan Gustafsson, and Michael Ljungberg
Manuscript submitted to *EJNMMI Physics*

**VI.** **Potential improvements to myocardial perfusion imaging using smaller pinhole apertures: A Monte Carlo investigation of the GE Discovery NM 530c SPECT system**
Mikael Peterson and Michael Ljungberg
Manuscript

# List of Contributions

**Paper I**

I designed the measurement setup, performed the measurements, and was the main author of the manuscript.

**Paper II**

I designed the InSPECT system, including the detector arrangement and the centrepieces, and performed the measurements. I was the main author of the manuscript.

**Paper III**

I planned the study, performed the pinhole simulations, and evaluated the results. I was the main author of the manuscript.

**Paper IV**

I performed the point-source measurements used for the validation of the simulated spatial resolution and system sensitivity and analysed the measurement results. I wrote parts of the manuscript and reviewed and commented on the rest of the manuscript.

**Paper V**

I generalised the back-projector algorithm, wrote the code, and performed the measurements and subsequent reconstructions. I co-authored the manuscript.

**Paper VI**

I planned the study, generated the anthropomorphic data sets, and performed the simulations and reconstructions. I was the main author of the manuscript.

# Introduction and Aims

> 'Eighty percent of success is showing up'.
>
> **Woody Allen**

Tomographic nuclear medicine imaging is the process of determining the three-dimensional (3D) *in vivo* distribution of a radiopharmaceutical to acquire diagnostic or therapeutic information regarding a biological system. A general tomographic nuclear medicine imaging system used for single-photon detection has three essential components: an image-forming element (collimator), an image detector, and a reconstruction algorithm. The imaging system performance is determined by how well these components interact and the limitations of each component.

Historically, photon detection has been performed using a gamma-camera system with a combination of scintillation detection and parallel-hole collimation. In this type of system, the spatial resolution and counting efficiency have an inverse relationship such that they can never be improved simultaneously. Thus, the optimisation task is to design an imaging system with an adequate resolution and efficiency, ideally allowing for a short imaging time and low administered radiation dose. In conventional gamma-camera imaging, a large detector area is desirable since the field of view (FOV) is determined by the physical size of the scintillation detector. Therefore, clinical systems based on parallel-hole collimation are large by necessity.

An alternative to conventional collimation is the use of a single pinhole or multiple pinholes. Historically, pinhole collimation has been utilised for applications that require high spatial resolutions within small FOVs, such as thyroid imaging. This objective is typically achieved by using a pinhole–detector combination that produces images with large magnifications. However, detectors of different sizes can be utilised because pinhole collimation allows for either minification or magnification of the projected image on the detector surface, enabling the system compactness or resolution, respectively, to be improved. In addition, the pinhole efficiency is distance-dependent ($\propto \text{distance}^{-2}$), and placing an object close to a

pinhole will yield an efficiency equal to or better than that of a parallel-hole collimator but at the cost of reducing the FOV. In short, pinhole collimation enables the use of various imaging geometries with different detector performance demands.

The revitalisation of pinhole collimation was driven by the pre-clinical imaging of human disease models in rodents, and this technique is currently employed in a commercial clinical system dedicated to myocardial perfusion imaging. Pinhole collimation is fundamentally different from conventional gamma-camera imaging with parallel-hole collimators and therefore requires adaptation and development of new concepts and models. Monte Carlo photon tracking programs such as SIMIND enable modelling and characterisation of the image formation process in nuclear medicine imaging systems. By simulating the imaging process, it is possible to estimate parameters that cannot be measured and to make changes to the (virtual) instrumentation to obtain an optimal design prior to building an actual prototype.

The aims of this research were

I. to design and construct a pre-clinical imaging system, InSPECT, based on photon-counting video detectors with pinhole collimation;
II. to incorporate and validate a pinhole collimator routine in the Monte Carlo program SIMIND before employing it to evaluate a new pinhole collimator material;
III. to validate a CZT semiconductor detector model used in the SIMIND program by performing experimental measurements;
IV. to develop and validate a Monte Carlo-based iterative pinhole reconstruction routine; and
V. to utilise Monte Carlo simulations and anthropomorphic computer phantoms to investigate the improvements in myocardial perfusion imaging that could be realised by improving the spatial resolution by using smaller pinhole apertures.

Our overall aim was to provide a validated simulation tool suitable for the characterisation and development of existing and future gamma-ray imaging systems with pinhole collimation.

# Pinhole Imaging

> 'Depends on da man. Depends on da hat'.
>
> **Spike Lee when asked 'What does a hat say about a man?'**

In nuclear medicine, radioactive substances are administered to patients for diagnostic and therapeutic purposes. A diagnostic procedure typically involves injection (or occasionally indigestion) of a radiopharmaceutical, followed by an examination. During the examination, a detection device is used to detect and/or map the origin of the emitted radiation.

One of the key advantages of nuclear medicine is the combination of sensitive radiation detectors and labelling radiopharmaceuticals with a high specific activity (i.e. large fractions of the injected pharmaceutical molecules are labelled with radioisotopes). Thus, high-quality imaging can be performed with small physical amounts of radiopharmaceuticals, leaving the functions of the biological system unaffected (Meikle et al. 2005, Cherry et al. 2012).

The types of examinations range from uptake measurements to gamma-camera studies, where the latter are intended to map the *in vivo* distributions of radiopharmaceuticals. The gamma camera (also referred to as a scintillation camera or an Anger camera) was designed and developed in the 1950s by Hal O. Anger (1967). In a chapter on radioisotope cameras, Anger described the scintillation-camera principles and two collimation techniques, namely, parallel-hole (then termed multi-channel collimator) and pinhole collimation (Anger 1952, Anger 1958).

The camera design proposed by Anger with multiple photomultiplier tubes (PMTs) coupled to a sodium-iodine scintillation crystal doped with thallium (NaI(Tl)) has remained essentially unchanged since its introduction, and most modern gamma cameras are based on the same principle. Typically, a gamma camera is assumed to employ a NaI(Tl) scintillation detector and parallel-hole collimation. The acquired images are two-dimensional (2D) projections of 3D activity distributions. The corresponding 3D activity distributions can be estimated by reconstructing multiple projections

acquired at different angles. This procedure is called single-photon emission computed tomography (SPECT).

The success of gamma cameras can be attributed to their usability in a wide range of imaging procedures from planar renal and bone scans to cardiac perfusion and cerebral blood flow SPECT. Noteworthy clinical exceptions to this general-purpose approach are thyroid (Hurley et al. 1971, Freitas et al. 1994) and parathyroid (Freitas et al. 1994, Kettle et al. 2006) imaging using pinhole collimation. These two procedures require sub-centimetre spatial resolutions. As shown in figure 1, pinhole collimation enables source distribution magnification but at the expense of reducing the FOV. In conventional gamma-camera imaging, the relationship between the source and the projected distribution size is always unity, whereas it depends on the source-to-pinhole and pinhole-to-detector distances in pinhole collimation. Consequently, pinhole collimation is better suited for tasks requiring focused high-resolution imaging.

## Principles of pinhole imaging

A pinhole is small round hole or aperture in an opaque material that functions as a primitive lens since only photons emitted within a certain solid angle are projected through the aperture. This phenomenon occurs frequently in nature, where pinholes serve as lenses in primitive eyes. For example, the eyes of giant clams, *Tridacna maxima*, include several hundred pinholes to project light onto light-sensitive cells (Land 2003).

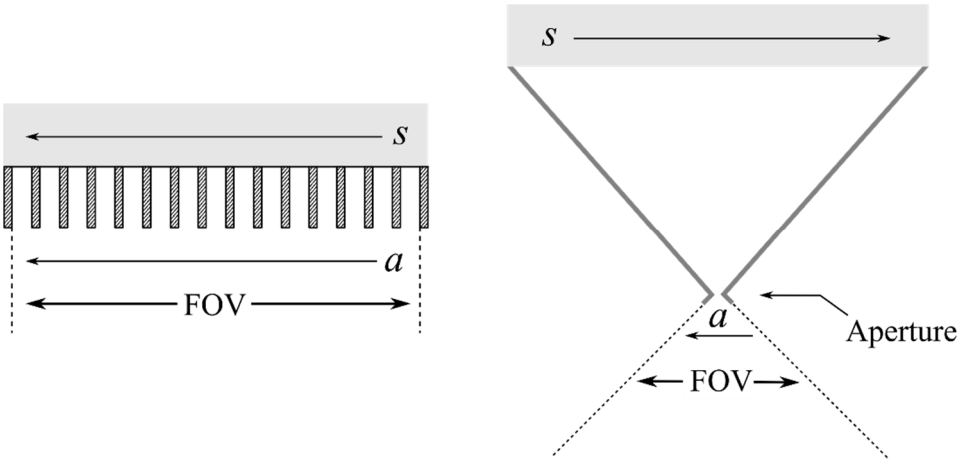


**Figure 1.** Cross-sections of parallel and pinhole collimation, where $a$ represents the position of a radioactive source, and $s$ is the mean position of the detector response. The arrows represent source translation and the resulting detector response translation. The parallel-hole collimator consists of several circular holes that selectively pass photons with directions nearly perpendicular to the detector surface. There is no magnification, and a source translation in any source plane corresponds to a translation in the detector plane of equal magnitude and direction. In a pinhole collimator, all photons pass through a single aperture. Consequently, the size of the FOV changes with the source-to-pinhole distance. A translation in a source plane corresponds to an opposite translation in the detector plane. In addition, the magnitude of this opposite translation depends on the magnification.

Several types of pinhole designs exist (van Audenhaege et al. 2015), two being knife-edge and channel pinholes. In the latter case, the actual pinhole is elongated into a channel, whereas a knife-edge pinhole can be seen as a special case of a channel pinhole with zero channel height. Channel pinholes can be useful if it is important to minimise the number of penetrating photons, e.g. for the imaging of high-energy photon emitters such as $^{131}$I, but this minimisation is achieved at the expense of decreasing the lateral sensitivity and contrast (van der Have et al. 2006). Other pinhole types have been developed, e.g. square loft-holes to maximise the detector utilisation of multiple pinholes (Deprez et al. 2013) and clustered pinholes to minimise penetration and enable the single-photon imaging of positron emitters (Goorden et al. 2010). In the works described in this dissertation, only knife-edge pinholes were considered.

Both Anger (1967) and Paix (1967) formulated models of the knife-edge pinhole efficiency $S$ and resolution $R_c$. In these models, only the photons that pass through the aperture, called the geometric component, are considered. The geometric sensitivity of a pinhole depends on the aperture diameter $d$, the angle of incidence $\theta$, and the distance between the pinhole and the source $h$, as defined in figure 2. The use of only the geometric component causes both the efficiency and resolution to be underestimated since penetration through the pinhole edge is not accounted for. Therefore,

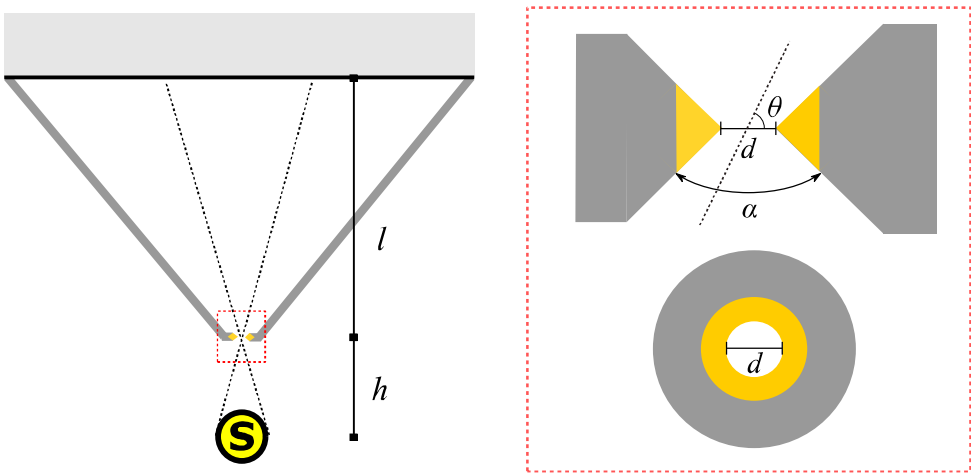


**Figure 2.** Schematic of the pinhole and an enlarged view of the pinhole aperture. The yellow markings indicate the areas in which penetration and scatter are the most critical. A source distribution, denoted by **S**, is projected through the pinhole onto the detector. In this process, the directions are inverted. Note that if $l < h$, the projected image will be reduced in size.

Anger defined a slightly larger effective aperture diameter $d_{\text{eff}}$ to account for penetration. $d_{\text{eff}}$ is a function of the geometric diameter, attenuation coefficient $\mu$, and acceptance angle $\alpha$:

$$d_{\text{eff}} = \sqrt{d[d + 2\mu^{-1}\tan(\alpha/2)]}. \qquad (1)$$

When using the effective aperture diameter, the pinhole efficiency is given by

$$S = d_{\text{eff}}^2 \frac{\sin^3\theta}{16h^2}. \qquad (2)$$

In this expression, the incident-angle-dependent sensitivity is modelled by a $\sin^3\theta$ term. In practice, the angular dependence is best modelled by $\sin^x\theta$, where $x > 3$, and the choice of $x$ depends on both the photon energy and aperture design (Smith et al. 1997). However, a more accurate analytical expression for the pinhole sensitivity that accounts for penetration through the pinhole edges has been derived (Metzler et al. 2001).

The pinhole resolution is defined as the lateral distance between two point sources when their projections onto the detector are tangent to one another.

The projection width is determined by the effective aperture diameter and projection magnification:

$$R_{\mathrm{c}} = d_{\mathrm{eff}} \frac{l+h}{l} = d_{\mathrm{eff}} \left(1 + \frac{1}{m}\right). \qquad (3)$$

The projection magnification $m$ is the ratio between the detector-to-pinhole distance (focal length) $l$ and the source-to-pinhole distance $h$. Thus, $R_{\mathrm{c}}$ is the minimal distance between two point sources that enables separate detection. This definition of the resolution does not take into account the changes in the spatial resolution due to the lateral position. As with the sensitivity, more detailed analytical expressions for the pinhole resolution that more accurately model the photon penetration and spatially variant response have been derived (Metzler et al. 2002, Accorsi et al. 2004).

From equation 2, it is clear that the efficiency increases with decreasing source-to-pinhole distance. In fact, the efficiency can exceed that of a parallel-hole collimator under certain conditions (Jaszczak et al. 1994, Weber et al. 1994). The resolution also improves simultaneously but at the cost of reducing the FOV, and the lowest theoretical planar resolution is determined by the aperture diameter. Thus, for small-animal imaging, in which interesting physiological and pathophysiological processes occur at sub-millimetre scales, sub-millimetre aperture diameters are required.

Equation 3 shows that the collimator resolution depends on the magnification factor, and the system resolution $R_s$ can be approximated as the sum in quadrature of the intrinsic and collimator resolutions (Beekman et al. 2007, Cherry et al. 2012):

$$R_{\mathrm{s}} = \sqrt{\left(\frac{h}{l} R_{\mathrm{i}}\right)^2 + R_{\mathrm{c}}^2}. \qquad (4)$$

Theoretically, a small high-resolution detector can be used with a smaller magnification to achieve the same efficiency and spatial resolution as a large low-resolution NaI(Tl)-scintillation detector. In fact, the number of independent measurements that a detector can make is more important than the detector size when using pinhole collimation. This performance measure is called the space–bandwidth product $S_{\mathrm{SBW}}$ and is defined as the maximum number of independent measurements that can performed on a detector surface (Barrett et al. 2005). $S_{\mathrm{SBW}}$ can be expressed as

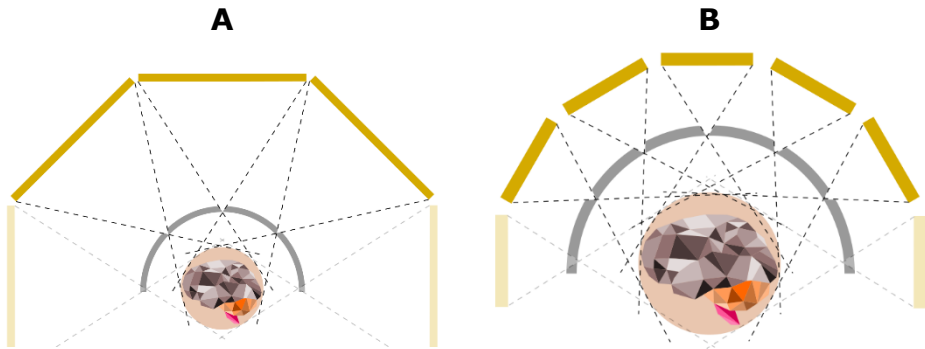


**Figure 3.** Dependence of the maximum number of detector–pinhole units in a system on the intrinsic resolution of the detector. With high-resolution detectors, more detectors can be packed closer together while retaining the resolution or efficiency of a single detector–pinhole unit. In each image, the FOV is depicted as a circle around the brain, with the detectors and pinhole material being yellow and grey, respectively. For a fixed system resolution, the increase in the sensitivity is proportional to the increase in the number of detector–pinhole units. An additional benefit of using high-resolution detectors is the increased angular sampling in the case depicted in (**B**) relative to (**A**). The images were redrawn from Rogulski et al. © (1993) IEEE.

$$S_{\mathrm{SBW}} = \frac{A_{\mathrm{D}}}{A_{\mathrm{El}}}, \qquad (5)$$

where $A_{\mathrm{D}}$ is the detector area, and $A_{\mathrm{El}}$ the area of the smallest resolvable element or point spread function (PSF) area. Since pinhole collimation enables image magnification/minification, $S_{\mathrm{SBW}}$ is a more relevant measure of the detector performance than the intrinsic resolution or size alone. Rogulski et al. (1993) demonstrated that improving the intrinsic resolution of a detector can improve both the spatial resolution *and* counting efficiency for non-multiplexing imaging. This paradoxical conclusion can be understood by viewing figure 3, where detectors with high intrinsic resolutions can be placed closer to the pinhole because of the lower magnification, thereby enabling more detectors and pinholes to be employed simultaneously. Regardless of $S_{\mathrm{SBW}}$, the employment of smaller detectors enables the use of a higher packing fraction and smaller system.

Another benefit of using more detectors in parallel is that doing so increases the number of projections that can be acquired simultaneously. Comparing figures 3A and 3B, images can be acquired from more angles in the latter case, and to achieve identical angular sampling in the two cases, the detector or object must be rotated in the scenario depicted in figure 3A. If sufficiently small detectors with sufficient resolutions are employed, it is possible to achieve ample angular sampling with a stationary system.

## Pinhole PSF

Equations 2 and 3 demonstrate that the sensitivity and resolution depend on the source position within the FOV, meaning that the collimator–detector response is spatially variant. The response of the detector system to a point source is described by the PSF of the system. An example of the spatial variation of a simulated PSF is provided in figure 4. A detailed analytical model for pinhole PSF has been developed (Metzler et al. 2002, Accorsi et al. 2004), and it includes a geometric term and the penetration through the pinhole edges. This analytical model is not a complete description of the imaging process since it does not include the photon interactions in the patient, the scatter in the collimator, or the instrument-specific parameters (such as the spatial and energy resolutions).

The collimator–detector response can be determined more accurately by performing Monte Carlo simulations of the imaging process. In simulated projection images, it is possible to separate components that would be difficult to model analytically using other techniques, such as the contribution from photons scattered in the object or the collimator. Although accurate, Monte Carlo simulations are computationally intensive and have historically been associated with long simulation times, but the increase in computational power over time and the development of more efficient simulators have decreased the simulation times.

Photons passing a collimator can be categorised as geometric, penetration, or scatter. The geometric photons are those that pass through the pinhole aperture, whereas the penetration and scatter components are those photons that pass through the collimator material without or with Compton interactions, respectively. The amplitude of each component is determined by the attenuation properties of the pinhole material and the pinhole design. For a given photon energy, the total cross section increases as the atomic number or density increases, thereby decreasing the amounts of penetration and scatter. Conversely, for a given material, an increase in the photon energy increases the relative contributions of penetration and scatter. The spatial distributions of these components for a $^{99}Tc^{m}$ point source imaged with 0.3 mm gold and Rose's metal pinholes are provided in figure 5 as examples.

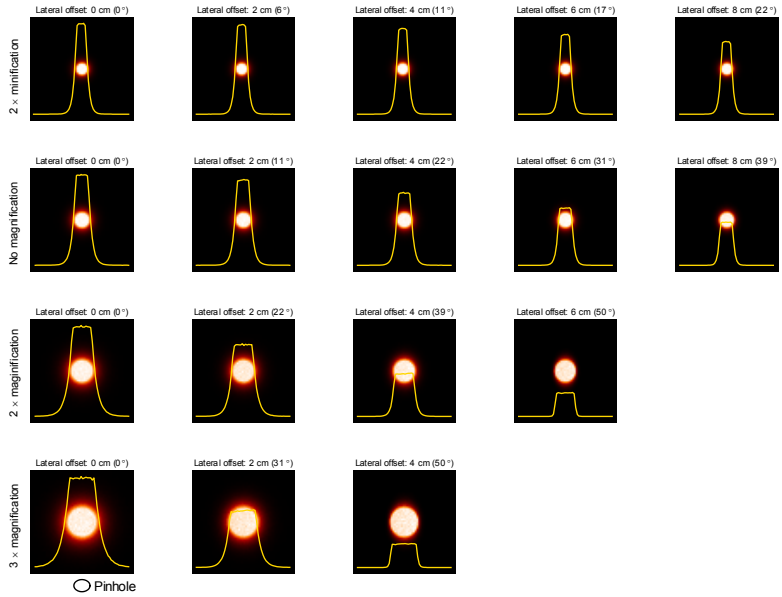


**Figure 4.** Simulated PSFs for a point source located in air with different source–collimator (vertical) and off-axis (horizontal) distances. The left-most column shows the PSFs for sources located along the pinhole axis, and each subsequent column was obtained by performing a 2 cm lateral translation. Starting at the top row, the sources were placed at distances from the pinhole that provided magnification by 0.5, 1, 2, and 3 times. The resulting incident angle is indicated in parentheses above each image. The images are positioned with the pinhole located in the bottom left corner. A profile is overlaid on the PSF in each image. Each profile is normalised to the maximum value in the entire data set; hence, the area under the curve reflects the total efficiency. In contrast to the PSF of a parallel-hole collimator, which is considered to be spatially invariant in planes parallel to the detector surface, the PSF of a pinhole is a function of both the incident angle and source-to-pinhole distance. The simulated opening angle was 110°, thus incident angles above 55° are excluded.

As the aperture size decreases, the penetration-to-geometric ratio increases, which limits the potential increase in the resolution compared to an impermeable pinhole. It is possible to suppress the penetration and scatter components by adapting alternate pinhole designs. As previously mentioned, the use of a channel pinhole instead of a keel edge reduces the penetration- and scatter-to-geometric ratios but can simultaneously reduce the contrast, especially for photons with large angles of incidence (van der Have et al. 2006). The same article also emphasised the importance of using a minimal acceptance angle $\alpha$. The same conclusion was also reached by us, as reported in Paper III (Peterson et al. 2015).

Another means of suppressing collimator penetration and scatter is the use of high-density materials with high atomic numbers, such as gold and platinum. These materials are expensive and therefore are not optimal as bulk collimator materials. One solution is to use gold or platinum for the

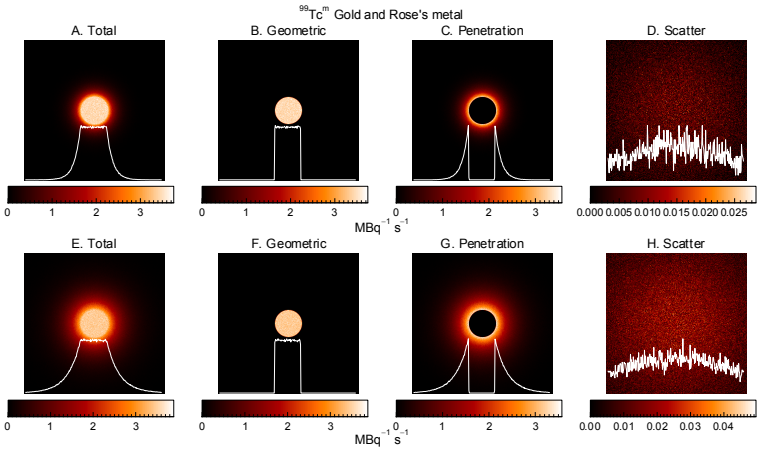


**Figure 5.** Spatial distributions of the geometric, penetration, and scatter components for 0.3 mm gold (A–D) and Rose's metal (E–H) pinholes. Rose's metal has a lower density and atomic number than gold, which translates into higher penetration and scatter contributions and decreases the resolution. The degenerative effect on the resolution can clearly be seen by comparing the penumbra widths of the penetration components of the two materials (C and G). The scatter component is relatively evenly distributed, although it is centred over the geometric centre. The scatter-to-total ratio is larger for Rose's metal than for gold, which is represented here as a higher probability. Each pixel value indicates the probability per unit activity and time (MBq$^{-1}$ s$^{-1}$).

keel only (see the yellow portion in figure 2), e.g. to incorporate gold or platinum pinholes into shielding materials such as tungsten (van der Have et al. 2009), tungsten epoxy (Miller et al. 2009), or Rose's metal (Peterson et al. 2010).

# Tomographic pinhole imaging

Early tomographic pinhole imaging studies focused on tracer imaging in small animal models such as rats (Jaszczak et al. 1994, Weber et al. 1994) and rabbits (Palmer et al. 1990) using clinical scintillation cameras with single pinholes. In the years that followed, the desire to perform high-resolution *in vitro* studies of human diseases in small animals led to the development of new detector types (Peterson et al. 2011) and novel pinhole designs (van Audenhaege et al. 2015).

The tomographic acquisition of multiple projections, i.e. pinhole SPECT with a single pinhole, is time-consuming and tedious, especially if acquiring a full-sized animal FOV, owing to the low efficiency when the object-to-pinhole distance is large. For a given object-to-pinhole distance, there are

two possible methods of increasing the system efficiency and/or detector utilisation: (1) increasing the number of pinholes per detector and/or (2) increasing the number of detector–pinhole units. Theoretically, two-fold increases in the numbers of pinholes and detector–pinhole units would yield identical increases in efficiency.

Multi-pinhole collimators have been implemented in two ways (Rowland et al. 2008): with non-overlapping and overlapping projections. In the former case, the pinholes are arranged so that the source projections do not overlap, whereas in the latter case, a varying fraction of projections overlap, or multiplexing, is present. Since our work focused solely on non-overlapping single-pinhole systems, multiplexing multi-pinhole systems will not be discussed further, but it should be noted that even though multiplexing can potentially increase the overall efficiency, the transformation of the overlapping data into artefact-free projections is not at all straightforward (Van Audenhaege et al. 2015).

Several preclinical SPECT systems with pinhole collimation have been developed and commercialised: Nano-SPECT (Forrer et al. 2006), U-SPECT-II (van der Have et al. 2009), U-SPECT-Vector (Goorden et al. 2013), and X-SPECT (Schramm et al. 2003). Deleye et al. (2013) performed an extensive evaluation of some of these systems, comparing the sensitivity, spatial resolution, uniformity, and contrast recovery for several isotopes. The reconstructed spatial resolution was reported to range from 0.58 mm to 0.69 mm when a 1 mm pinhole was used. The sensitivity was in the range of 0.06%–0.39%[1].

Owing to the attractive characteristics of SPECT imaging with pinhole collimation, i.e. a high resolution and high sensitivity within a relatively small FOV, this technique has been and still is implemented when designing new clinical systems. The limited FOV restricts the application of such systems to organ-specific imaging, and commercial systems tend to be designed to focus on large patient groups to justify the purchase of dedicated SPECT scanners rather than conventional gamma cameras. A recent example of a clinical pinhole SPECT system is the dedicated myocardial SPECT scanner called GE Discovery NM 530c (Bocher et al. 2010). Combined with solid-state detectors, it offers a compact, stationary system capable of increasing patient throughput and lowering the doses administered to patients (Herzog et al. 2010). Another system is the

[1] The sensitivity was measured with a point source located at the centre of the FOV. The system with the highest sensitivity is designed with a small FOV and must scan several neighbouring FOVs to acquire a full body scan. Thus, the entire body acquisition time reduction does not necessarily scale linearly with the sensitivity.

G-SPECT scanner, which is a dedicated neuro-imaging scanner with 54 pinholes placed in a circular bore with a diameter of 40 cm (Ljungberg et al. 2017). Although not yet commercially available, the preliminary results indicate that this scanner could both decrease the acquisition time and increase the spatial resolution. Plans exist to introduce a second, larger bore that would enable whole-body pinhole imaging. In theory, such systems should offer specifications superior to those of conventional gamma-camera systems and, in terms of spatial resolution, even positron emission tomography (PET) scanners.

# Detection Principles of Pinhole Imaging

> 'Aziz, Light!'
>
> **Professor Pacoli in the movie 'The Fifth Element'**

Photon detection is an essential step in tomographic nuclear medicine imaging, together with image formation (collimation) and image reconstruction. In a conventional gamma camera, detection is performed using a NaI(Tl) scintillation detector. Following the interaction in a NaI(Tl) crystal, scintillation light is emitted by the de-excitation of electrons from dopant sites, which are introduced by adding small amounts of thallium dopants to the crystal (Knoll 2010). The scintillation light propagates through a light guide and spreads out over a PMT array, and the deposited energy is calculated by summing the signals of all PMTs. The interaction location can be determined by calculating the centroid of the signal distribution over the PMTs. The energy resolution is typically 9–10% for 140 keV photons with a 70–90% photopeak efficiency that depends on the crystal thickness (Cherry et al. 2012). Overall, a NaI(Tl) scintillation camera is an efficient photon detector, and when combined with a parallel-hole collimator, it provides a versatile detector system that is the 'work-horse' in nuclear medicine departments worldwide.

A detector is typically characterised by a number of parameters. An ideal detector is inexpensive and mechanically robust, has a uniform response, and can perfectly determine the interaction location (both the in-plane location and depth) and photon energy. Moreover, the detector performance should be independent of the orientation of the detector relative to the earth's magnetic field (Peterson et al. 2011).

The determination of the ideal detector size is not straightforward because it depends on the choice of image-forming element. A large detector with a low resolution might be preferable to a smaller detector with an equal number of resolvable elements, which is true for gamma cameras since the

NaI(Tl) detector size ultimately determines the maximum FOV. However, for pinhole collimators, the two detectors are theoretically interchangeable, although their levels of magnification differ. Thus, the number of resolvable elements per unit detector surface area becomes relevant when specifying the detector performance (Barrett et al. 2005). This key figure of merit is called the space–bandwidth product and was defined in the previous chapter, as was the concept of using compact high-resolution detectors in combination with pinholes to increase the system resolution and sensitivity simultaneously.

## Scintillation light detection

Many photon detection approaches involve the detection of scintillation light generated following a photon interaction in a scintillator. The purpose of a scintillation light detector is to convert the weak light output of a scintillation pulse into a measurable current pulse without adding detrimental amounts of noise. Historically, PMTs have been the most used devices in gamma cameras, especially in combination with NaI(Tl).

Charge-coupled devices (CCDs) provide an alternative to PMTs. The basic idea is to photograph an irradiated scintillator screen and perform readout on a frame-by-frame basis. This setup enables each photon interaction in a frame to be identified and processed individually (Beekman et al. 2005).

PMTs and CCDs will be discussed further in this chapter, but some other notable scintillation light detectors should be mentioned. These include two types of photodiodes: avalanche photodiodes and silicon photomultipliers (Roncali et al. 2011). The latter have been used in commercial PET systems together with a lutetium-yttrium oxyorthosilicate scintillation crystal and are also promising for use in PET/magnetic resonance (MR) systems (Vandenberghe et al. 2015).

### PMTs

A PMT has two main components: a photocathode and a set of dynodes that are sealed in a glass vacuum chamber. A schematic of a PMT is provided in figure 6. For PMTs, the initial conversion of scintillation light into charge carriers (photoelectrons) is performed using a photocathode. The quantum efficiency (QE) of a photocathode is defined as the number of photoelectrons emitted per incident scintillation photon, and the QE of a photocathode is

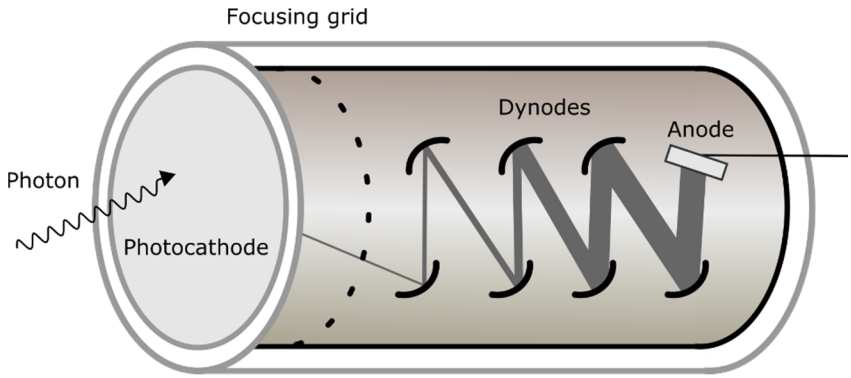


**Figure 6.** Schematic of a PMT. The dark grey line represents the electron path when travelling between dynodes. At each dynode, there is a multiplication of the number of electrons as each accelerated electron collides with the dynode, generating several secondary electrons that are then accelerated towards the next dynode, where each electron generates new electrons upon impact.

determined by its material properties, i.e. the absorption of scintillation light, electron migration, and the surface escape potential. The maximum QE among common photocathodes is 20%–30% (Knoll 2010). Additionally, the QE varies with the wavelength of the incident scintillation light, and care must be taken to achieve sufficient overlap between the scintillation light emission spectrum and the spectral sensitivity of the photocathode. Contrary to photocathodes, photodiodes have high QEs.

Following the generation of photoelectrons in a photocathode, the emitted photoelectrons are accelerated and focused on the first of a set of dynodes, and multiple secondary electrons are generated upon impact with each dynode. The new photoelectrons are then accelerated towards and focused on the second dynode, and the process is repeated for all dynodes (typically 8–12 in total). Finally, the electrons are directed towards an anode where the magnified charge is collected. Typically, the PMT signal gain is on the order of $10^8$ (Knoll 2010). The most relevant downside, with respect to imaging, of using PMTs is that the relative uncertainty in the total signal increases with each multiplication step. This uncertainty will degrade the ability of the gamma camera to determine the total deposited energy, which is assumed to be proportional to the sum of the signals generated in all PMTs. Even though PMTs contribute to the uncertainty in the energy estimate, the overall uncertainty in the energy estimate is primarily determined by the limited number of generated scintillation photons. The consequence of the poor energy resolution is that it is more difficult to discriminate the scattered photons within the photopeak window. Scattered photons are detrimental to the overall image quality because they provide

erroneous spatial information and their contribution to the full photopeak window should be minimised.

## Video detectors

Instead of using a PMT as a scintillation light detector, a scintillation crystal can be filmed using a CCD detector. The CCD detector readout is on a frame-by-frame basis, rather than being event-based, as is the case with PMTs. Hence, the photon interactions will be visible as flashes in a single frame, as illustrated in figure 7. This characteristic enables photon counting, i.e. the identification of individual events in a frame. With photon counting, the interaction position can be determined more accurately by calculating the centroid position for each event, which increases the already high intrinsic resolution of the video detector (Beekman et al. 2005). Following a study in which a CCD detector was coupled to a caesium-iodine (CsI(Tl)) scintillator with coded aperture collimation, it was reported that an estimated decoded resolution of 30 μm was achieved for planar imaging but with a limited FOV (Miller et al. 2008). Additionally, it is possible to estimate the deposited energy by summing the signals for each event, but generally, the energy resolution is poor relative to that of a gamma camera (Miller et al. 2006).

Compared to other scintillation light detectors, CCDs offer higher QEs, but the signal extraction is hampered by electronic noise. To increase the signal strength to above the noise threshold, CCD cooling and signal amplification have been suggested. Two examples of such methods are electron-multiplied CCDs (Jerram et al. 2001) and the inclusion of image intensifiers (Miller et al. 2006). The latter approach has been used to develop detectors with $S_{BW} > 2{\times}10^5$ (Miller et al. 2009), which is approximately a factor of 10 better than that of a conventional gamma camera (Peterson et al. 2011).

Some CCDs operate at frame rates greater than 100 frames/s. Therefore, large amounts of data must be processed efficiently and/or stored for post-processing. For example, events can be identified using efficient event-labelling algorithms, and data can be stored as list-mode files (Miller et al. 2008). A dedicated animal brain SPECT scanner with 20 CCD-based detectors and real-time graphics-processing-unit-assisted reconstruction has been developed (Miller et al. 2009, Miller et al. 2011).

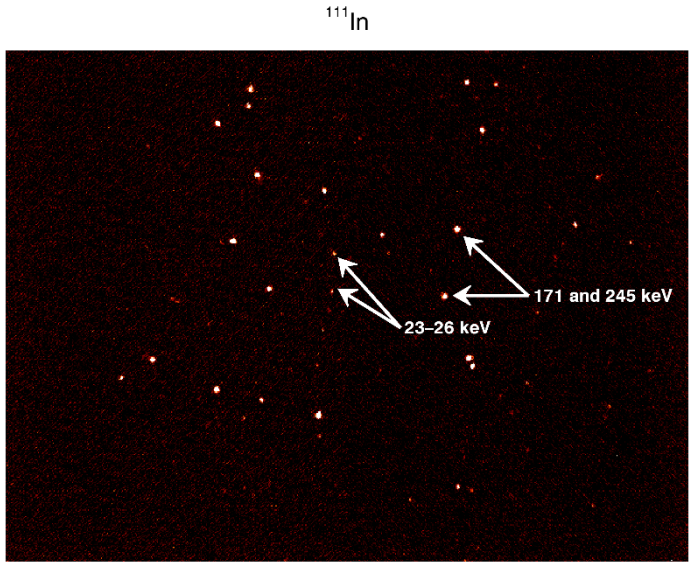


**Figure 7.** Single frame from a video-based detector equipped with a CsI(Tl) scintillator. The detector was irradiated by gamma rays and x-rays from $^{111}$In. Each frame can be parsed to localise individual events, which is called photon counting. This technique enables energy separation by summing the signals of individual events, demonstrated here by the difference between the intensities of the gamma rays (171 keV and 245 keV) and characteristic x-rays (23–26 keV).

# Semiconductor photon detection

Semiconductor technology is one of the main alternatives to scintillation-based photon detection. Photon detection with a semiconductor is different from scintillation-based detection in that the charge induced by the gamma-ray interactions is read out directly. Direct conversion into a measured current reduces the number of random processes (e.g. light generation, propagation, and amplification for NaI(Tl)). Each of these steps increases the relative uncertainty in the number of signal carriers, thus degrading the overall energy resolution compared to that of a direct converting detector.

When a photon interacts in a semiconductor material, electrons are elevated to the conduction band and leave vacancies, or holes, in the valence band. An electrode current is induced when the electron–hole (e-h) pairs move towards the anode and cathode, respectively, as depicted in figure 8 (Shockley 1938, Ramo 1939). Thus, this process is different from the classical

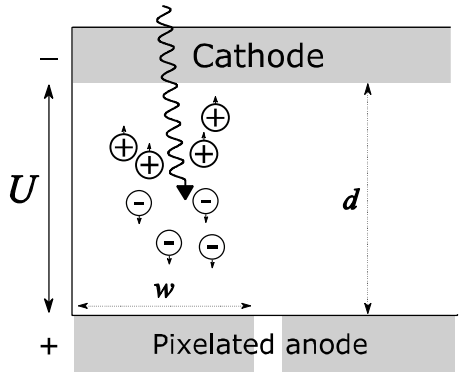


**Figure 8.** Schematic of the charge collection process in a semiconductor detector of thickness $d$ with an applied voltage $U$. The holes migrate towards the cathode, whereas the electrons migrate towards the pixelated anode with a square side length of $w$. Note the gap between the anode elements.

charge collection process in a NaI(Tl) camera. The number of charge carriers generated in a semiconductor depends on the size of the band gap and deposited energy. An ideal semiconductor imaging detector would have a bandgap that is sufficiently small to enable numerous charge carriers to be elevated to the conduction band and sufficiently large to prevent thermally induced elevation (Knoll 2010), thus operating at room temperature.

When the electrons and holes move in the semiconductor material, they are hindered by impurities and interactions with phonons, and the terminal velocity is determined by the product of the field strength $E$ and the mobility factor $\kappa$. A second effect that influences the e-h mobility is trapping at impurities and lattice defects. Given a mean free time $\tau$ (lifetime), the electrons and holes will travel a mean distance of $E\kappa\tau$ if it is assumed that no de-trapping occurs (Barrett et al. 2005).

When used for imaging, solid-state detectors can be pixelated by assigning an array of individual readout electronics to each element of a partitioned anode. The detector thickness must be at least few millimetres to achieve adequate photon absorption, and the anode pixels should be small to maximise $S_{\mathrm{BW}}$. A drawback of using smaller anode pixels is the increased charge sharing between them. An initially compact charge cloud will be dispersed owing to the concentration gradient, Coulomb repulsion, and trapping (Gros d'Aillon et al. 2006). Therefore, charge sharing sets a lower limit on the anode pixel size and thus limits the maximum number of detector elements per unit detector area.

Table I. Important properties of semiconductor materials used for SPECT at relevant photon energies. Adapted from Peterson et al. (2011).

| | Density ($g\ cm^{-3}$) | Att. at 140 keV ($cm^{-1}$) | Energy per e-h pair (eV) | Mobility × lifetime | |
|---|---|---|---|---|---|
| | | | | Electron ($cm^2\ V^{-1}$) | Hole ($cm^2\ V^{-1}$) |
| Si | 2.33 | 0.02 | 3.61 | 0.42 | 0.22 |
| Ge | 5.32 | 0.72 | 2.98 | 0.72 | 0.84 |
| CdTe | 5.85 | 3.22 | 4.43 | $3\times10^{-3}$ | $5\times10^{-4}$ |
| CdZnTe | 5.82 | 3.07 | ~5 | $3\times10^{-3}$ | $5\times10^{-5}$ |
| $HgI_2$ | 6.40 | 8.03 | 4.20 | $<10^{-2}$ | $5\times10^{-5}$ |

## CZT detectors

Several semiconductor materials have been suggested for use in photon detection, and the properties of some of them are listed table I. Si and Ge both have excellent energy resolutions and charge-transport properties; however, Si suffers from low attenuation, and Ge must be used in a cryogenic state because of its small band gap. Materials such as mercuric iodide ($HgI_2$), cadmium telluride (CdTe), and cadmium zinc telluride[2] (CZT) offer wider bandgaps (low background signals at room temperature) and sufficient intrinsic peak efficiencies[3]. Compared to Si and Ge, the charge carriers in CZT are less mobile and have higher probabilities of recombination at nearby impurities and defects. A useful feature of CZT is that the detection of photons is not affected by the presence of strong magnetic fields, which enables simultaneous SPECT/MR imaging (Rittenbach et al. 2013).

In CZT, the drift length of electrons is larger than the typical detector thickness[4] $d$ ($\kappa_e \tau_e E \gg d$), whereas it is short for holes ($\kappa_h \tau_h E \ll d$) owing to their low mobility–lifetimes product (Barrett et al. 2005). Electrodes are primarily sensitive to charge carriers that move within the electrode width $w$ from the electrode. If the anode is large compared to the CZT thickness, the anode sensitivity is uniform for a charge moving within the CZT crystal. Thus, the total signal is proportional to the sum of the hole and electron drift distances within the material. Since the drift length of the holes is short (and the electrons are likely to traverse the entire active detector volume) a

[2] $Cd_{1-x}Zn_xTe$, where $x$ is the fraction of zinc, typically ranging from 0.04 to 0.2.

[3] Ratio between the counts in the full-energy peak and the number of photons incident on the detector surface (Knoll 2010).

[4] ~0.5 cm for CZT in the GE Discovery NM 530c.

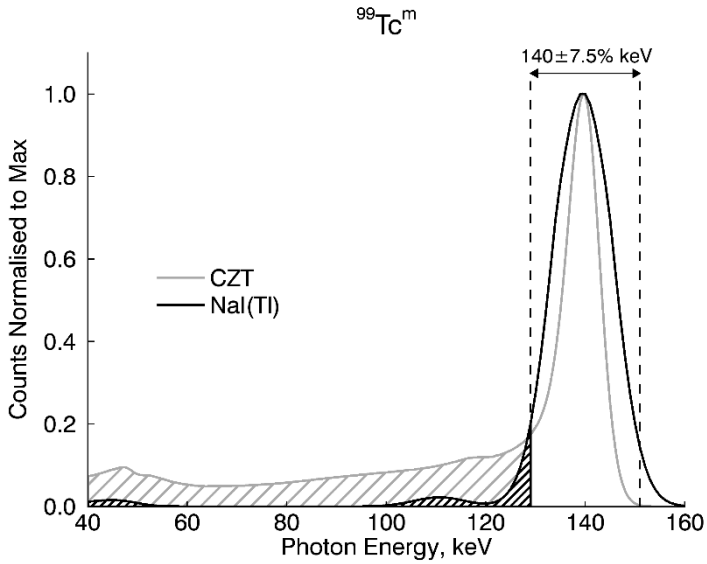


**Figure 9.** Normalised pulse height spectrum for 140 keV photons from a source in air for collimated CZT and NaI(Tl) detectors. The CZT (grey) spectrum has a characteristic low-energy tail outside the photopeak window, which is due to charge sharing and depth-of-interaction (DOI) effects. The spectra were obtained by performing SIMIND simulations.

DOI effect will be introduced for interaction depths that exceed the hole drift length.

The DOI effect can be counteracted by pixelating the anode, i.e. decreasing $w$, and thus, also the sensitive volume of each anode element. The electron cloud with its high average drift length will traverse the now smaller volume, whereas the holes will move away from the anode; thus, their contribution to the anode current will be negligible. Consequently, the signal becomes less dependent on the interaction depth and hole trapping when the anode is pixelated. This phenomenon is called the small-pixel effect (Barrett et al. 1995), and the result is that more full-energy depositions are placed correctly in the pulse height spectrum when the anode pixel size decreases.

In practice, a decrease in the anode pixel size increases the charge sharing between anode pixels from charge dispersion owing to the initial concentration gradient, Coulomb repulsion, and trapping (Gros d'Aillon et al. 2006). The total deposited energy could theoretically be determined by summing the signal over several anode pixels, although the summation is complicated by the presence of electronic noise and the gap between the anode pixels (Wangerin et al. 2011). Basing the estimate of the deposited

photon energy on the detected current in a single-anode element leads to general underestimation of the photon energy, even for full-energy events. The effect of charge sharing is manifested in the pulse height spectrum as a registration of full-energy depositions in the energy bins below the photopeak window (figure 9). The pulse height characteristics will depend on the ratio of the thickness to the anode pixel size, $d/w$. However, regardless of the choice of $d/w$, a fraction of full-energy events will always populate the low-energy part of the pulse height spectrum. For a more rigorous approach to gamma detection with semiconductors, the reader is referred to Barrett et al. (2004).

# SPECT Systems in this Dissertation

> 'Let's use this setback to our advantage'.
>
> **Skipper Skip-King, Madagascar 2**

This chapter introduces the two tomographic SPECT systems used to perform the research described in the papers included in this dissertation, namely, the pre-clinical system InSPECT and myocardial perfusion imaging system GE Discovery NM 530c.

## InSPECT system

Papers I and II focus on the development of a small-animal SPECT imager with the working name InSPECT. The project was a collaboration with the Center for Gamma-Ray Imaging at the University of Arizona, Arizona, USA. The collaboration involved the exchange of acquisition software and hardware relating to a CCD-based Bazooka detector (Miller et al. 2006, Miller et al. 2012). The detector name is derived from the apparent similarity between an early prototype and a bazooka rocket launcher.

The Bazooka detector consists of five components: a scintillator, an image intensifier, spacer rings, a lens, and a camera with a CCD sensor. A schematic of the system is provided in figure 10. In short, the scintillation light emitted from the photon interaction point in the scintillator is multiplied using a micro-channel plate within the image intensifier. The magnified light signal is then imaged by a CCD sensor focused on the intensifier output window.

Our detectors can be equipped with two types of scintillators: plastic scintillators (Lanex™, from a radiology screen) or custom-made columnar CsI(Tl) scintillators. Both types of scintillators are circular with 50 mm

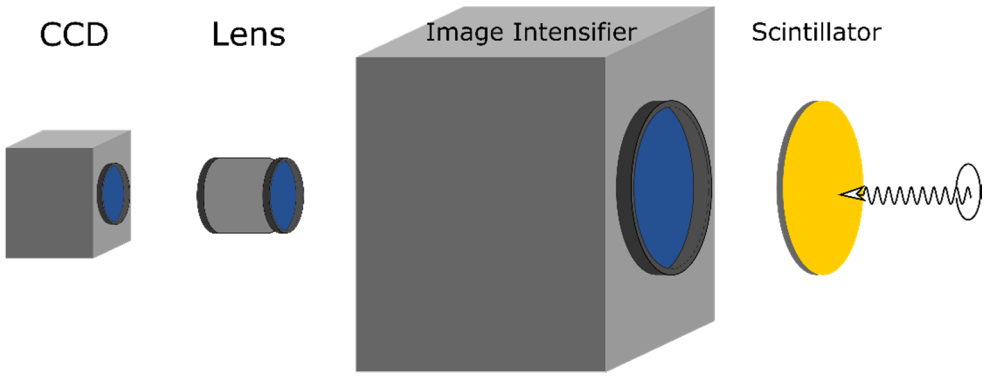


**Figure 10.** Separated view of the Bazooka SPECT detector components. Collimated photons interact in the scintillator material, and the scintillation light intensity is multiplied before being imaged by a CCD sensor. In the actual setup, spacer rings are positioned between the lens and the image intensifier, but they are not shown in this image. Neither is the scintillator cover, which prevents stray light from entering the image intensifier.

diameters that match the image intensifier input window. CsI(Tl) is both thicker and denser (0.4 mm thick and with a specific density of 4.51 (Knoll 2010)) than Lanex™ (~0.1 mm thick and with a specific density of 1.03) and has a greater overlap between the scintillation light emission spectrum and the S25 photocathode sensitivity of the image intensifiers. Additionally, CsI(Tl) has a higher probability for photoelectric interaction and a higher scintillation light output. Therefore, the individual light flashes are easier to separate from the CCD background noise and from the flashes generated by the spontaneous emission of photoelectrons from the photocathode. Lanex™, on the other hand, is easy to handle and can be cut from a large Lanex™ sheet from an x-ray cassette into a shape that matches the image intensifier input window.

The image intensifier, a Philips X1335 military surplus image intensifier, consists of a photocathode at the entrance window that releases electrons when irradiated by (scintillation) light. The photoelectrons are then accelerated towards a micro-channel plate. The micro-channel plate consists of a bundle of glass tubes, and each tube acts as an individual electron multiplier, analogous to a single PMT. A potential is applied across the length of a single tube, and secondary electrons are generated when electrons strike the inner surface of the tube. These are in turn accelerated by the potential difference and give rise to a cascade of electrons. The resulting electron multiplication depends on the angle and position of the entering electron relative the tube (Knoll 2010), which may explain the relatively poor energy resolution achievable using this technique (Miller et al. 2006).

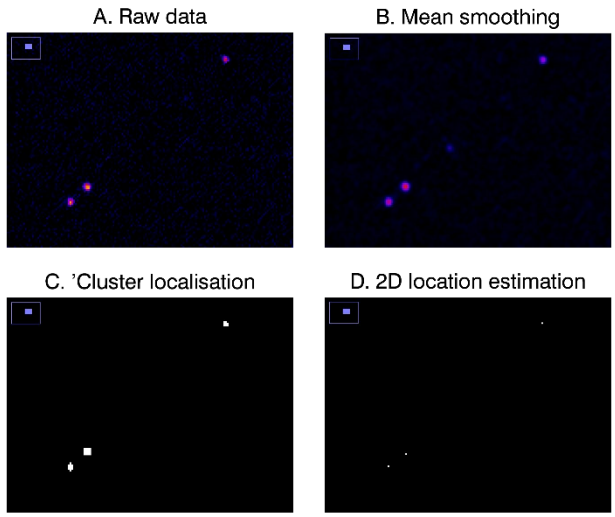


**Figure 11.** Frame-parsing algorithm used by the Bazooka SPECT detector. The raw data (A) is initially smoothed (B); then, each event is indexed by performing a fast forward–backward raster scan (C), and the event interaction position is assumed to have the same pixel coordinates as the maximum value within the event (D). The centroid position estimates within a frame are then used to increment the same positions in a centroid sum image. The use of only the centroid position to define the position improves the intrinsic spatial resolution of the detector (Beekman et al. 2005). The location and total pixel signal within an event are also stored separately in a listmode file for potential post-processing.

Finally, electrons from the micro-channel plate create light flashes as they interact in the phosphorous (ZnCdS:Ag) screen.

Image frames of the phosphorus screen are acquired using a Point Grey Research© Grasshopper camera, which acquires 640×480 pixel image frames at a rate of 60 frames/s. Each frame is processed on the fly, and the algorithm includes the identification and separation of individual events (Miller et al. 2012). Each image frame is smoothed using a mean filter prior to setting all values less than a user-defined threshold to zero. Individual events are labelled by performing a fast forward–backward raster scan (Suzuki et al. 2000), and the location of the maximum value within the cluster is assumed to be the interaction position. The algorithm is demonstrated in figure 11 for a sub-portion of the detector surface.

## InSPECT design

InSPECT was designed to house eight Bazooka detectors, each with a single pinhole for photon collimation. A schematic of an InSPECT detector–pinhole unit is depicted in figure 12. The individual projection magnification

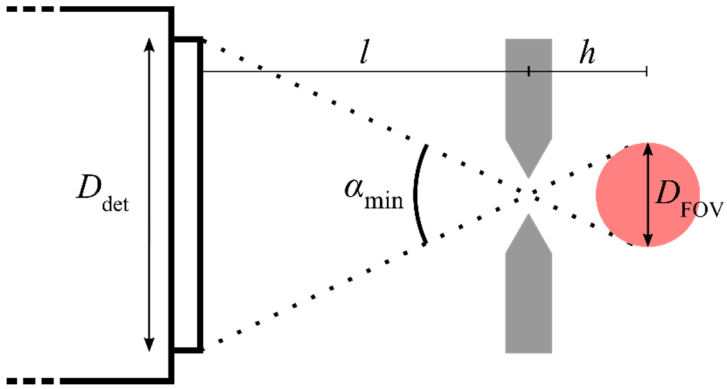


**Figure 12.** Detector–pinhole configuration used for the eight detector–pinhole units in the InSPECT system. The system design is based on a desired 20-mm-diameter FOV indicated by the red circle and a central bore radius of 30 mm. $\alpha_{\min}$ is the smallest opening angle that does not block potential photon paths.

$m$ of an InSPECT detector–pinhole unit can be calculated from a chosen FOV diameter $D_{\mathrm{FOV}}$ and the detector diameter $D_{\mathrm{det}}$. The detector diameter is determined by the physical size of the image intensifier input window. $D_{\mathrm{FOV}}$ is the diameter of a spherical FOV and is defined as 20 mm. This FOV size was selected to enable high-resolution imaging of the brain or kidneys of a mouse. With a detector size of 50 mm, the magnification is given by

$$m = \frac{D_{\mathrm{det}}}{D_{\mathrm{FOV}}} = \frac{l}{h} = 2.5. \tag{6}$$

We defined a bore size suitable for mouse imaging to be 60 mm ($2h$). Thus, the distance between the detector and pinhole $l$ can be calculated as follows:

$$l = mh = 75 \text{ mm}. \tag{7}$$

The relative amount of penetration increases with increasing $\alpha$. Therefore, $\alpha$ should be set as small as the detector dimensions allow (van der Have et al. 2004, Peterson et al. 2015). The minimal acceptance angle is determined by

$$\tan\frac{\alpha_{\min}}{2} = \frac{D_{\mathrm{det}}}{2l}. \tag{8}$$

For a desired FOV of 20 mm, $\alpha_{\min} = 38.9°$, and the acceptance angle was therefore set to 40°.

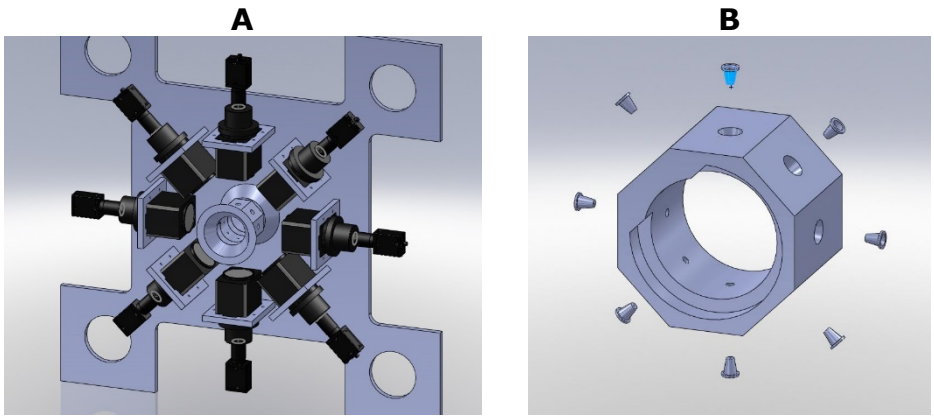


**Figure 13.** (A) InSPECT detector arrangement and pinhole central region. Eight Bazooka detectors are arranged in a circle with 2.5 magnification focused on a spherical FOV with a diameter of 20 mm. (B) The central region that contains the pinholes is made from Rose's metal, a high-density alloy with a low melting point that enables high-precision casting and machining. Individual pinholes are formed separately and cast into an insert that is then mounted in the central piece, as shown in (A).

Figure 13 shows the InSPECT detector arrangement and pinhole housing. In total, eight detector–pinhole units are mounted in a ring within the pinhole housing. In addition to housing the pinholes, the central ring also shields the detector from photons and must therefore be made from a dense material with a high atomic number. One such material is Rose's metal, an alloy composed of 50% bismuth, 28% lead, and 22% tin. Rose's metal has a low melting point and does not contract while cooling, making it suitable for casting objects of various shapes. When Rose's metal is solid, it can be machined with a high precision. The casting and machining of the central pieces of the InSPECT system are described in Paper II. Initially, InSPECT was equipped with platinum pinholes with 0.3 mm apertures, but the system can also be fitted with Rose's metal pinholes. Relative to other pinhole materials, e.g. gold (van der Have et al. 2009) and platinum (Miller et al. 2009), Rose's metal has a lower density and atomic number and consequently a higher fraction of photons penetrating and scattering from the pinhole edges. In Paper III, we will discuss the consequences of using Rose's metal as a pinhole material in terms of the penetration- and scatter-to-total ratios and their effects on the PSF width (Peterson et al. 2015).

InSPECT projection data were reconstructed using a ray-tracing algorithm based on the same method used in the back-projector mentioned in Paper V, and the reconstructed slices of clinical $^{57}$Co point-source measurements are presented in figure 14. With the high spatial resolution of the InSPECT system, the source is not a point; instead, the activity is distributed along the edges of a 3.5-mm-diameter hole, as is evident in the reconstructed slices.

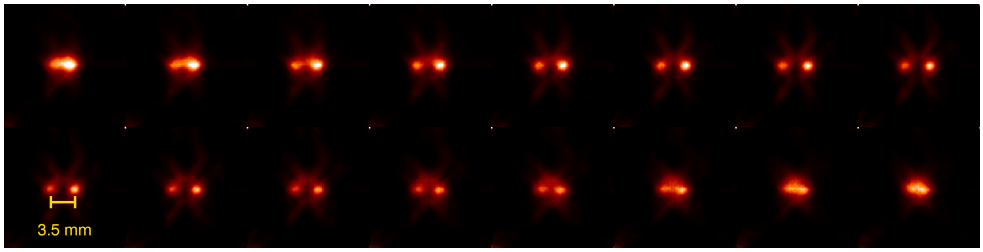


**Figure 14.** Sixteen consecutive reconstructed slices of a clinical point source. The activity of the point source is located along the wall of a 3.5-mm-diameter hole, as is evident in the reconstructed images. The reconstructed slice thickness is 0.32 mm, and the in-plane voxel size is 0.2 mm.

Of course, this distribution has little, if any, effect on the clinical usage as a point source owing to the coarse resolutions of gamma cameras, but it demonstrates the high resolution achievable with InSPECT.

We did not characterise the spatial resolution or sensitivity of InSPECT due to a combination of instrument failure and a low counting efficiency. The two most notable reasons were (1) the background contribution of spurious events due to thermal emission of photoelectrons from the photocathode, which are inseparable from events following photon interactions, and (2) the low efficiency caused by the plastic scintillator used in InSPECT. Apart from being thinner and having a lower density than CsI(Tl), Lanex™ yields a scintillation light emission spectrum that overlaps less with the photocathode efficiency spectrum, thus decreasing the overall light output for each event at the image intensifier output window and making it more difficult to separate the spectrum from the CCD background and spurious events.

## GE Discovery NM 530c

As previously described, new types of solid-state detectors are used in dedicated cardiac SPECT systems with either pinhole (Bocher et al. 2010) or parallel-hole collimation (Gambhir et al. 2009). Papers IV–VI describe the use of SIMIND to simulate one of these systems, GE Discovery NM 530c (henceforth abbreviated as NM 530c).

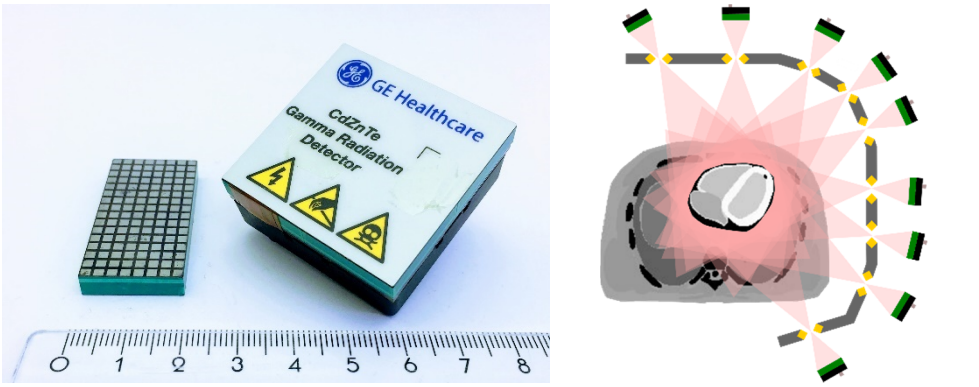


**Figure 15.** Individual CZT module with 16×16 elements. A full detector is composed of four modules with a total of 32×32 elements. Shown next to the detector is a portion of the CZT detector, where 8x16 anode elements are visible. The small size of the detector compared to those of scintillation-based detectors enables the fabrication of compact stationary system designs. NM 530c is based on CZT detection with pinhole collimation. Detector–pinhole units are focused on a circular FOV, and an artistic rendition of the system is shown on the right, where the green and black units represent the CZT detectors. NM 530c has a focused FOV in which the patient heart is centred.

NM 530c consists of 19 CZT detectors, each with a single pinhole for image formation. Each detector surface is divided into 32×32 elements by pixelating the anode (each with side lengths of 2.46 mm) and has readout electronics for each anode element. Thus, each element is an individual detector, and the pixel size is equal to the anode size. A positive consequence of the dedicated circuitry is that the CZT detector is linear even at high count rates (Bocher et al. 2010). In practice, the 8×8 $cm^2$ CZT detector consists of four separate modules, each 4×4 $cm^2$. A module is depicted in figure 15 together with a sample of an exposed CZT anode.

The energy resolution of the CZT detector is better than that of a conventional NaI(Tl) scintillation detector, resulting in lower contamination of scattered events in the photopeak. The high energy resolution also improves the energy peak separation when performing dual-isotope imaging, e.g. during a $^{201}Tl$ and $^{99}Tc^{m}$ 1-day protocol (Ben-Haim et al. 2016). However, as previously explained, the contamination of $^{99}Tc^{m}$ events in the $^{201}Tl$ photopeak window will occur owing to effects relating to the charge transport.

The detector–pinhole units are arranged in a semicircle around the patient, providing a total angular coverage of approximately 180°, and reconstruction is performed with 19 projections. As a result, the detector–pinhole units remain stationary during image acquisition. A scanner bed is used to position the patient's heart in the FOV, as illustrated in figures 15 and 16. The FOV is approximately a sphere with a diameter of 19 cm. Further, as discussed in

**Figure 16.** GE Discovery NM 530c SPECT camera. The patient lies on a scanner bed in either a supine or prone position, and the scanner bed is moved so that the heart is placed at the centre of the FOV. After the patient has been positioned (right image) and acquisition has started, there is no detector motion. A second version of the system, Discovery NM 570c, is equipped with a computed tomography (CT) scanner for localisation and attenuation correction. Images used with permission of GE Healthcare.

Paper IV, the sensitivity and resolution vary over the FOV, but the spatially variant PSF is taken into account during the reconstruction (Bocher et al. 2010). Clinical image reconstruction is performed with a 3D iterative Bayesian reconstruction method using a modified EM algorithm (Hebert et al. 1989) with a one-step-late Green's prior for noise regularisation (Green 1990). The reconstructed images have 4 mm voxels and 70×70×50 matrices.

Paper IV discusses the implementation of a mathematical model of the CZT detection process in the Monte Carlo program SIMIND, which can be used to model the image formation process accurately and enables the separation of the individual components that together form the final projection images. The simulated projections can be used to obtain realistic measures of clinically relevant parameters, e.g. the number of scattering events in the photopeak window. Myocardial perfusion imaging with a gamma camera is a well-established technique, and inevitably, the introduction of the new pinhole-based system will challenge some conventional practices regarding, for example, attenuation patterns (Timmins et al. 2015, Martinsson et al. 2016), patient positioning (Hindorf et al. 2014), and artefacts related to activity outside the FOV (Chan et al. 2016). Therefore, such a model is valuable for characterising this relatively new type of scanner system.

# Monte Carlo Simulations in Nuclear Medicine

> 'Do random events ever lead to concrete results? Seems unlikely – after all, they're random'.
>
> **Burger EB, Starbird MP. The Heart of Mathematics: An Invitation to Effective Thinking.**

In nuclear medicine, the Monte Carlo method can be used to simulate the physical processes of particles and photons traversing some media. One example of such use is the simulation of radiation transport during nuclear medicine imaging, which involves the simulation of the histories of numerous individual photons, each emitted from a pre-defined source distribution, and their transport through an inhomogeneous medium until their (potential) detection. The Monte Carlo method determines the fates of photons by using random numbers to sample stochastic events (interaction type, changes in photon direction, etc.) from different probability density functions (PDFs).

For example, when modelling photon transport, the PDFs used to sample a photon path length are based on the attenuation coefficient per unit length, as described by $\mu e^{-\mu x}$ (see the left graph in figure 17), where $x$ is the distance travelled by the photon, and $\mu$ is the energy- and material-specific linear attenuation coefficient. The linear attenuation coefficient is the sum of all photon cross sections for the relevant interactions. When sampling a photon path length, a random number between 0 and 1 will determine the path length from the cumulative PDF (CPDF) shown in the right image in figure 17.

In practical terms, the simulation process starts with the initiation of a photon with a sampled direction and given energy. After travelling the sampled distance, the photon is either within the object or has escaped it. In the former case, the type of photon interaction is determined using a sampling procedure similar to that described above. The predominant interactions for the photon energies used in typical nuclear medicine

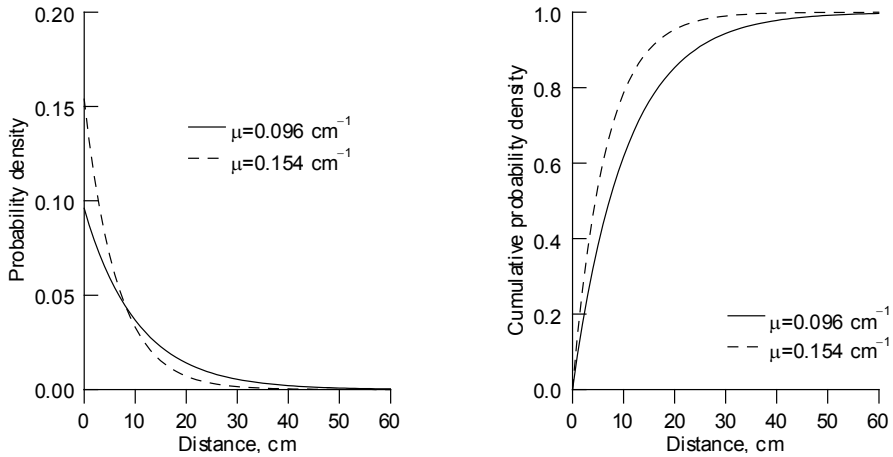


**Figure 17.** Two exponential PDFs and their respective CPDFs. Given a random number between 0 and 1, the CPDF can be used to sample the distance a photon travels in a homogenous medium. The attenuation coefficients are for 511 keV (0.096 $cm^{-1}$) and 140 keV (0.154 $cm^{-1}$) for photon attenuation in water.

procedures are photoelectric absorption and coherent and incoherent (Compton) scattering. For the latter, a new direction and photon energy can be sampled using a sampling method based on the Klein–Nishina cross section (Kahn 1956, Koral et al. 2013). Photons escaping the phantom will continue with unperturbed directions and energies and may reach the collimator surface where the photon transport and interactions in the collimator and detector are simulated. The photon is terminated when it is absorbed, detected, or exits the simulated geometry. The deposited energy and location of any interaction within the detector are stored together with the information regarding the photon history (e.g. whether the photon scattered in the patient or collimator). As this process is repeated, the estimated Monte Carlo image approaches a realistic estimate of the count flux over the detector surface. Since the number of simulated photons is always finite, the estimated count flux will vary between different simulations.

The final precision of the simulation results, assuming that the model is perfect, is primarily determined by the quality of the random number generator, the accuracy of the cross-section data, and the number of photon histories simulated. Since the simulation time scales linearly with the number of simulated histories, any increase in the precision requires more computational time or power. Conventional gamma-camera systems detect roughly 1 in every 10000 emissions; therefore, an analogous simulation would

have the same low efficiency in projection estimate generation. Therefore, an analogous approach would be very slow since a large number of detected histories would be required to achieve a reasonable precision.

Techniques intended to increase the efficiency of Monte Carlo simulations are referred to as variance reduction techniques owing to their common aim of minimising the count-flux variation between simulations with identical numbers of histories (Haynor et al. 2013). Instead of considering the photons to be discrete entities in the projection image estimate (count or no count), each photon is associated with an individual weight. An example of a variance reduction technique is the elimination of photon absorption in the object. Since attenuation in the object is undesirable from an efficiency standpoint, the history is not terminated when photoelectric absorption is sampled, but rather the weight is decreased by a factor equal to the absorption probability. Once detected, the pixel signal is increased by its weight rather than being incremented. Other variance reduction methods involve forcing the photon towards the detector (Ljungberg et al. 1991) and replacing the collimator with a convolution operation with a collimator–detector-response kernel (de Jong et al. 2001). The practical consequence of variance reduction is that the simulation time required to achieve a given precision dramatically decreases (Haynor et al. 2013). On the other hand, variance reduction techniques that are based on simplifications may increase the efficiency at the cost of accuracy in certain measurement situations, for example, if the collimator penetration is neglected in the collimator–detector-response kernel when performing $^{131}$I imaging (Liu et al. 2008).

Monte Carlo simulations are used in nuclear medicine to complement measurements because they can be employed to estimate parameters that are difficult or impossible to estimate using measurements only. Since the history of each simulated event is known, the final projection image estimate can be separated into different image components. One such example is shown in figure 5, where a point-source image is divided into components that have 1) passed through the pinhole aperture or 2) scattered in or 3) penetrated through the pinhole edges. Further differentiation among the image components is possible when the photon interactions in the patient are also included. For example, image scatter contributions are often estimated using Monte Carlo simulations (Frey et al. 1996, Beekman et al. 2002, Koral et al. 2013).

Monte Carlo simulations are also used to evaluate different collimator–detector designs, such as pinhole collimator designs, when developing new SPECT systems (van der Have et al. 2006, Goorden et al. 2010, Peterson et al. 2015). As such, they provide an inexpensive, flexible, and time-saving

alternative to constructing prototypes and physically modifying existing systems.

Other applications involve simulating the imaging of the activity distributed in (more or less) realistic computer phantoms. For example, these phantoms can be used to evaluate clinically relevant metrics (El-Ali et al. 2005, Brolin et al. 2013), to provide known source distributions for the comparison of reconstruction methods (Tsui et al. 1994), or to determine the accuracy of the calculations of the absorbed doses in radionuclide therapy (Brolin et al. 2015, Gustafsson et al. 2015).

## Monte Carlo programs in nuclear medicine imaging

A wide range of photon tracking Monte Carlo programs have been developed and are available to the research community. Some of these programs are designed for more general purposes and involve the simulation of both photon and charged particle transport (Jan et al. 2004, Wilderman et al. 2013, Salvat et al. 2014). Programs that are intended specifically for modelling photon transport during SPECT acquisition are typically more computationally efficient (owing to variance reduction techniques); however, this efficiency is achieved at the expense of a lower generalisability and flexibility compared to general-purpose programs. Several specialised photon tracking programs are available, such as SIMIND (Ljungberg et al. 1989), SimSET (Harrison), and UMCS (de Jong et al. 2001, Beekman et al. 2002), and of these three, the first and last have pinhole simulation capabilities.

In this work, we employed SIMIND to simulate image acquisition using pinhole collimation. Paper III discusses the validity of using SIMIND for pinhole modelling by comparing the analytically calculated and published penetration- and scatter-to-total ratios resulting from UMCS simulations (van der Have et al. 2004). Paper VI describes the implementation of a CZT detector model in SIMIND and a comparison of its results with measurements. The CZT model was used in the research presented in Papers V and VI.

# Modelling of CZT detection

The current induced in an electrode due charge motion in a vacuum is described by the Shockley–Ramo theorem (Shockley 1938, Ramo 1939), and the overall current depends on the particle velocity and charge and the strength of the electric field between the anode and the cathode. The electrode charge $\Delta Q_{\mathrm{E,k}}$ collected from an interaction point $k$ is described by the Hecht equation (Hecht 1932). If only the charge generated by moving electrons is considered, the total induced charge in the anodes is given by

$$\Delta Q_{\mathrm{E,k}} = \frac{\lambda_e^* N_{\mathrm{E,k}} q}{\tau_a} \frac{e^{\left(\frac{z-d}{\lambda_e}\right)}}{1 - e^{\left(-\frac{d}{\tau_a}\right)}} \times \left(1 - e^{\left(\frac{z-d}{\lambda_e^*}\right)}\right), \qquad (9)$$

where $N_{\mathrm{E,k}}$ is the number of created e-h pairs; $q$ is the electric charge of an electron; $d$ and $z$ are the material thickness and interaction depth (relative to the entrance surface), respectively; $\lambda_e$ is the mean free drift length of electrons (Guerra et al. 2008); and

$$\lambda_e^* = \frac{\lambda_e \tau_a}{\lambda_e - \tau_a}. \qquad (10)$$

The charge induction model can be derived using a number of approximations, specifically, that the anode sensitivity $\tau_a$ to moving particles or the weighting function can be approximated using an exponentially decaying function, the initial charge has an infinitesimal spread, and the function does not include cross-talk (moving charges generating signals in several anode pixels) or charge spread. From equation 9, it can be concluded that the induced current in the anode is proportional to the charge created, $N_{\mathrm{E,k}} \times q$ and thus to the deposited energy during the photon interaction.

The lateral spread of the charge cloud can be modelled according to a Gaussian distribution (Gros d'Aillon et al. 2006) with a standard deviation of

$$\sigma = \sqrt{\frac{4D(d-z)^2}{\mu U}}, \qquad (11)$$

where $\mu$ is the electron mobility, $D$ is the diffusion constant (Einstein 1905, Abe et al. 2005), and the $U$ is the applied voltage. This equation shows that

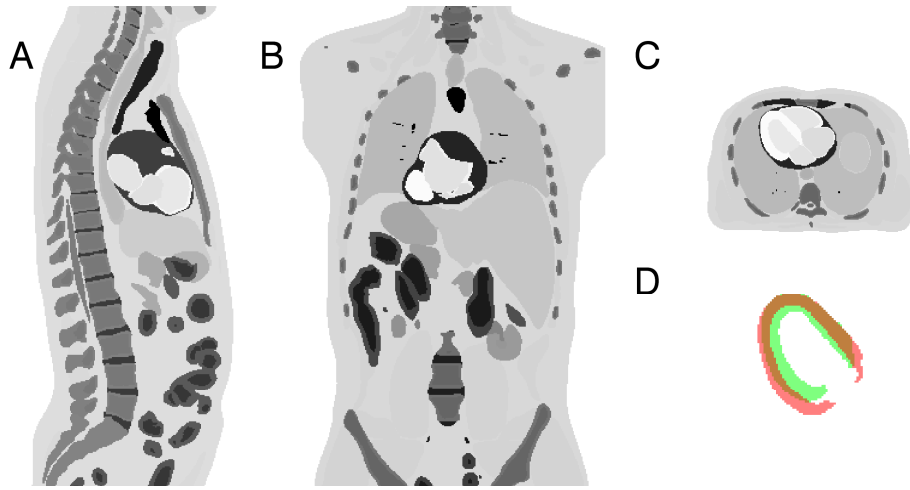


**Figure 18.** Sagittal (A), coronal (B), and transversal (C) slices through a voxelised XCAT phantom, which can be used to simulate cardiac and respiratory motion. The image in (D) shows transversal slices of the left myocardial wall at the end-diastole (red) and end-systole (green) time points. The greyscale value in the phantom does not represent the organ density but is a unique integer identifier for each object.

the cloud spread increases with the distance travelled and decreases when a higher voltage is applied. Consequently, when the interaction occurs above or close to an anode border, the calculated induced current (equation 9) will be shared between anodes. For a full-energy event close to the anode border, this current sharing will manifest itself as a count redistribution from the full-energy peak to the lower regions since only one of the anode elements is used for image formation and energy estimation. Finally, the energy resolution can be modelled as a convolution by both a detector-specific Gaussian function (Chen et al. 2008) and a second Gaussian that is chosen empirically.

## Anthropomorphic computer phantoms

The estimation of clinical parameters from simulated images requires the simulation of realistic patient-like computer phantoms. The early computer phantoms used in Monte Carlo simulations were, by necessity, of simple design, consisting of simple geometric shapes such as rods, cubes, or spheres that are easy to define mathematically. Consequently, early anthropomorphic phantoms were assemblies of organs with shapes defined

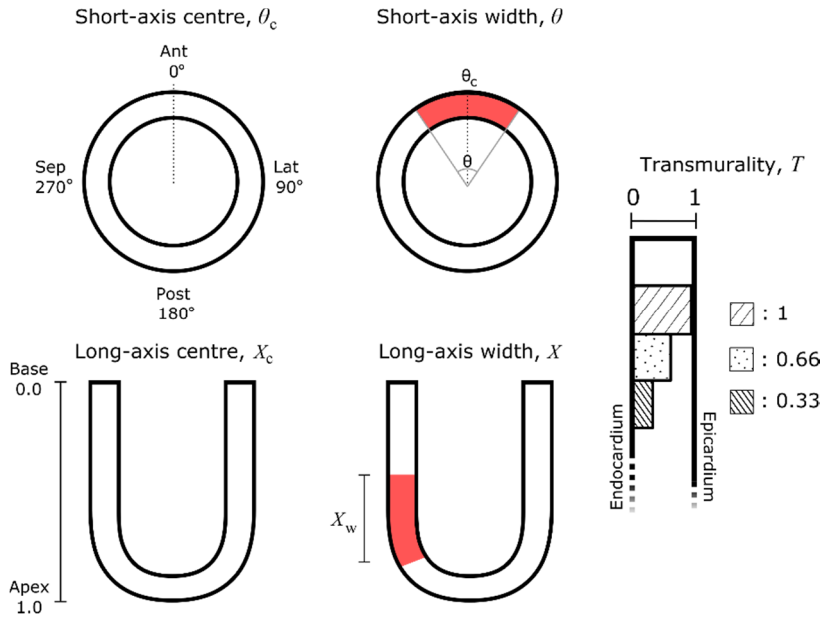


**Figure 19.** In the XCAT phantom, the extent of the myocardial lesions is specified by an angle in the transverse plane and an extent along the long axis. The transmurality of the lesion can also be specified.

by mathematical expressions (Snyder et al. 1978). Those phantoms were used to calculate population-based dose estimates, as the phantoms were assumed to represent organs with the average composition, size, and location among a population.

More realistic phantoms can be generated by segmenting patient images obtained via CT or magnetic resonance imaging by assigning unique numbers to the voxels within a structure that can later be used to specify the voxel tissue density and activity concentration within the structure. Even though they are realistic, voxel-based phantoms lack flexibility when simulating important image-degrading effects such as cardiac and respiratory motion. More realistic phantom behaviour can be achieved by using hybrid phantoms in which the structural surfaces are defined by non-uniform rational B-splines (Zubal et al. 2013). Phantoms belonging to the latest generation have extended flexibility, and changes can be made to their body and organ sizes as well as to their motion patterns (heartbeat and respiratory motion). Before performing a simulation, voxelisation of the surface-based phantom is necessary, hence the name hybrid phantom. Figure 18 shows a voxelised version of the extended cardiac-torso (XCAT) hybrid phantom (Segars et al. 2010).

Additionally, XCAT enables the user to add myocardial perfusion lesions, and each lesion is characterised by its circumferential and long-axis extents and transmurality (fraction of the wall), as shown in figure 19. Paper VI describes the use of an anthropomorphic XCAT phantom to emulate a realistic source and density distribution. A patient population was generated, where each patient had a beating heart (eight gates) but no respiratory motion, and each simulation was performed using a different perfusion lesion extent and transmurality.

# Iterative Tomographic Image Reconstruction

> 'Förståndet jagar oss. Men vi är snabbare'.
>
> **Toilet graffiti at Göteborg C**

The objective of tomographic nuclear medicine image reconstruction is to generate a 3D activity source distribution from a set of measured projections of that distribution. In modern SPECT reconstruction, iterative reconstruction methods such as maximum likelihood–expectation maximisation (ML-EM) (Shepp et al. 1982) and ordered subset–expectation maximisation (OS-EM) (Hudson et al. 1994) have replaced their analytical counterparts such as filtered back-projection to a great extent (Hutton 2011). The main advantages of ML-EM are the abilities to incorporate photon physics and position-dependent detector response functions into the system model. The algorithm is also based on the assumption that the measured projections are subject to Poisson noise, which improves the noise characteristics in the reconstructed images.

Typically, iterative reconstruction methods are more computationally demanding, and the computational effort increases with the complexity of the projector model. Nevertheless, with the increasing processing power of modern computers, iterative reconstructions methods are sufficiently fast to be used in clinical routine, even with rather complex models.

## ML-EM

The formation of a source distribution for projections requires a description of the imaging process, i.e. a model. For a single projection bin $i$, the number of registered counts $p_i (i = 1, 2, \ldots, M)$ from a source distribution is given by

$$p_i = \sum\nolimits_j a_{ij} f_j, \qquad (12)$$

where the system matrix element $a_{ij}$ describes the probability of detecting a count $p_i$ per source activity in a voxel $f_j (j = 1, 2, \ldots, N)$. As such, the intensity in a projection bin is the weighted sum of the activities in all of the source voxels. In other words, in this linear model, a decay in any source voxel may contribute to any projection bin. In contrast, in the model used in filtered back-projection, a bin only receives contributions from voxels intersected by a given line.

An iterative algorithm commonly used for reconstruction is the ML-EM algorithm (Shepp et al. 1982, Lange et al. 1984). The fundamental idea of ML-EM is to maximise the likelihood $\Pr(\mathbf{m}|\mathbf{f})$ of measuring the projections $\mathbf{m}$ from the source distribution $\mathbf{f}$ under the assumption that the photon counting process follows Poisson statistics. The algorithm used to maximise $\Pr(\mathbf{m}|\mathbf{f})$ is called expectation maximisation, and when it is applied to SPECT reconstruction, the algorithm is described by the equation

$$f_j^{\text{new}} = \frac{f_j^{\text{old}}}{\sum_i a_{ij}} \sum_i a_{ij} \frac{m_i}{\sum_k a_{ik} f_k^{\text{old}}}. \qquad (13)$$

This algorithm minimises the ratio difference between the measured $m_i$ and model estimated $p_i$ projections. Therefore, it is important for the imaging model $\mathbf{A}$ used to estimate $p_i$ to represent the actual image formation process accurately. The assumption is that if the measured and estimated projections are similar, then the measured and estimated source volumes will be similar also.

In equation 13, the value of the current voxel estimate $f_j$ is updated iteratively. Each iteration is started with a projection $\sum_k a_{ik} f_k^{\text{old}}$ of the current source estimate. There is no source estimate before the first iteration; thus, the reconstruction is started by providing a guess of the source estimate. The initial guess can be either a volume with uniform positive non-zero values or a more realistic source distribution, e.g. a source volume reconstructed using filtered back-projection.

Following the projection of the estimated source, the measured and estimated projections are compared by calculating their ratio. A significant deviation of the ratio from 1 indicates a large difference between $m_i$ and $p_i$. The projected ratio is then back-projected, and the back-projected ratio is multiplied by the current source estimate, which becomes the new source

estimate after applying the normalisation $1/\sum_i a_{ij}$. $\sum_i a_{ij}$ is the probability that a photon is detected in any of the bins. This process is then repeated for all of the source voxels, completing an iteration.

In ML-EM, maximisation of the log-likelihood is not correlated with an improvement in the image quality after a certain number of iterations because the measured data are often noisy; therefore, the source distribution that is the most consistent with the data also tends to be noisy (Barrett et al. 1994, Lalush et al. 2004). In general, there are two methods of addressing this problem: regularisation and stopping the iterative process prematurely. The noise in reconstructed images is regularised by applying an additional penalty term $U(\mathbf{f})$ in the log-likelihood function that penalises the differences between neighbouring values. Reconstruction algorithms based on this criterion are known as maximum *a posteriori* (MAP) reconstruction algorithms (Hebert et al. 1989). The goal is to penalise the presence of noise while still preserving the contrast, and when applying a penalisation term, the MAP-EM expression becomes

$$f_j^{\text{new}} = \frac{f_j^{\text{old}}}{\sum_i a_{ij} + \beta \frac{\partial}{\partial f_j} U(\mathbf{f})|_{\mathbf{f}=\mathbf{f}^{\text{old}}}} \sum_i a_{ij} \frac{m_i}{\sum_k a_{ik} f_k^{\text{old}}}, \qquad (14)$$

where $\beta$ determines the weight of the penalisation term relative to measured data. The behaviour of the penalisation and its effects on the final image are determined by $\beta$ and the somewhat subjectively chosen penalisation function. The penalisation function can include some prior knowledge about the source distribution, such as anatomical information (Dewaraja et al. 2010), and is therefore often termed a prior. Several different priors have been suggested, such as Gibbs priors (Hebert et al. 1989, Green 1990). When calculating the neighbourhood penalty using the previous source distribution $\mathbf{f}^{\text{old}}$, the method is referred to as a one-step-late method.

In ML-EM, the appearance of reconstructed images will be affected by the initial guess; for example, with a uniform guess, images will be biased towards uniformity. Thus, to improve noise characteristics, a smooth first estimate should be selected, and the iterative process should be stopped relatively early on the basis of a user-specified endpoint or some statistical measure (Hebert 1990). On the other hand, the exact stopping point is often determined using a task-based approach with regards to some image quality measure, i.e. by finding the setting that maximises the performance of an observer.

There are some practically relevant shortcomings of iterative SPECT reconstruction. For instance, the algorithm is slow compared to image reconstruction with filtered back-projection since it is computationally intense. The reconstruction time can be significantly shortened by updating the source estimate more frequently using only a limited number of projections, i.e. a subset. This algorithm is called OS-EM (Hudson et al. 1994).

The total number of elements in the system matrix is $M \times N$. Consequently, even for the relatively modest matrix sizes used in nuclear medicine, an uncompressed system matrix will require impractical amounts of memory if stored directly on a hard drive (Lazaro et al. 2005, Miller et al. 2011). In addition, the system matrix should ideally contain information regarding the photon interactions in the object as well as instrument-specific settings (e.g. the energy window setting); therefore, the system matrix should theoretically be recalculated and stored for each study to retain optimal reconstruction results. Typically, $a_{ij}$ is instead calculated during the forward- and back-projections instead of referencing a pre-computed system matrix, thus avoiding the large storage requirements.

## Compensation for image-degrading effects

As stated previously, the accuracy of the ML-EM image reconstruction results will ultimately be limited by the validity of the image formation model. Therefore, the model should correctly predict the distribution of the detected counts in the detection bins for a given source distribution. The simplest approximation, regardless of whether pinhole or parallel-hole collimation is being modelled, involves the assumption that all of the events in a detector bin originated from positions along a line of response. In the case of pinhole collimation, the line of response is determined by the bin position relative to the pinhole.

In SPECT, photon attenuation and scatter in the object affect the detected count distribution. Since attenuation decreases the number of detected events relative to the number of events for a non-attenuating object, attenuation correction will increase the signal. Scatter provides an additional contribution to the overall image; hence, scatter correction will decrease the signal. The effects of the two respective corrections can be seen in the reconstructed phantom data profiles in figure 20.

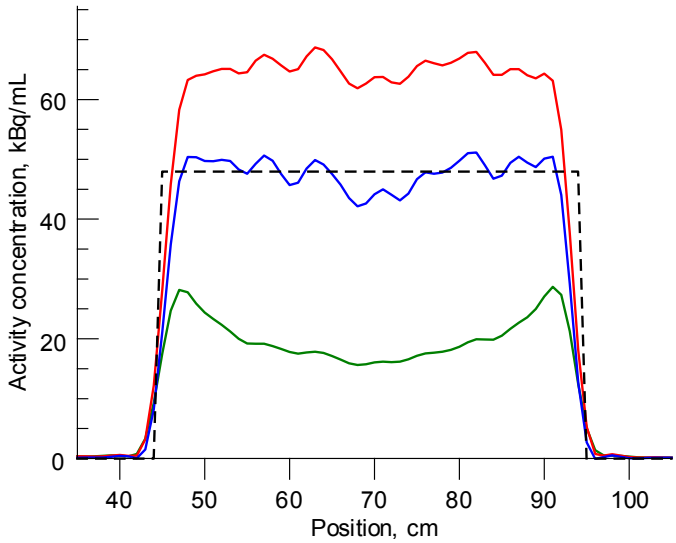


**Figure 20.** Profiles of a cylindrical phantom with a homogenous distribution of $^{99}Tc^{m}$ (48 kBq/mL). The profiles are the sums of several rows to minimise the influence of noise in the profiles. It is essential to include both attenuation and scatter to achieve a high quantitative accuracy. In the uncorrected profile, the activity concentration is underestimated, especially in the middle. The activity concentration decreases when compensating for the relatively uniform scatter contribution. The attenuation and scatter corrections were performed using CT and the dual-energy window (DEW) method, respectively.

Additional image degradation results from the limited spatial resolution caused by the imperfect detector resolution and non-ideal collimation. In emission tomography, where the system resolution is typically more than two times the voxel size, the limited resolution leads to a spill-over of counts into adjacent detector elements. In addition to affecting the spatial distribution of the detected counts, spill-over also causes underestimation of the activity concentration in small objects (Erlandsson et al. 2012), which is called the partial-volume effect (PVE) and also leads to loss of contrast.

## Attenuation

The simplistic line-integration model does not account for photon interactions in an object or a phantom. If photon attenuation is not included in the model, the estimated counts from deep-lying sources are underestimated relative to those from superficial sources. Attenuation can be corrected using the transmission information acquired by performing a

CT scan. The desired attenuation coefficients can be calculated from the CT density (Hounsfield units) and energy-specific look-up tables (Patton et al. 2008).

### Scatter

Photons that scatter before detection cause blurring of the projections, thus lowering the contrast of the reconstructed images (Hutton et al. 2011). When quantifying the activity concentration, the scatter component is particularly critical since as much as 40% of the projection counts can originate from scattered photons (Cherry et al. 2012). While SPECT attenuation correction is relatively standardised and straightforward when using CT information, scatter correction is implemented in a variety of ways (Hutton et al. 2011). In energy-window-based methods such as the DEW method (Jaszczak et al. 1984) and triple-energy-window method (Ogawa 1994), the scatter fraction in the photopeak window is estimated on a pixel-by-pixel basis by using the counts from one or two adjacent energy windows. In general, these methods are easy to implement and have a reasonable accuracy (Ljungberg et al. 1994). An alternative to measuring the scatter contribution is to perform model-based correction, e.g. to use Monte Carlo simulations (Frey et al. 1996, Beekman et al. 2002).

If the estimated scatter data are implemented using simple projection subtraction, negative projection counts may result, which is both unphysical and a violation of the fundamental ML-EM assumption of non-negative counts that follow a Poisson distribution. Instead, scatter data can be included as an additive term in the forward-projection step (Beekman et al. 1996, Beekman et al. 1997, King et al. 1997), meaning that it is not necessary to model the scatter in the projector and that there is no risk of negative projection values.

### Spatial resolution

The aim of partial-volume correction is to reverse the redistribution of the signal in the source distribution that is caused by the imperfect system resolution. Partial-volume correction can be performed using post-reconstruction deconvolution techniques or by including the detector–collimator response function, i.e. the PSF, into the reconstruction model (Erlandsson et al. 2012). Compensating for the detector–collimator response

in the reconstruction can improve the image quality but has also been shown to introduce ringing artefacts (Tsui et al. 1994).

### Monte Carlo simulation of the system matrix

A full Monte Carlo simulation of the system matrix is theoretically the most accurate description of the imaging process. Image reconstruction using system matrices calculated by employing Monte Carlo methods have been performed for both parallel-hole collimators (Lazaro et al. 2005, Ouyang et al. 2007) and pinholes (Aguiar et al. 2014). In practice, it means that a point source is simulated on a voxel-by-voxel basis and that the respective PSFs are stored and loaded during the reconstruction process. Consequently, either a significant time or processing power is necessary to simulate every position. Ideally, the system matrix should include information regarding the attenuation and scatter in the object. A patient-specific matrix can be calculated by including the patient composition in the simulations, but such a procedure would require a large storage capacity (in addition to a long simulation time).

## Pinhole image reconstruction

One of the first published examples of pinhole SPECT reconstruction was performed using divergent back-projecting algorithms (Palmer et al. 1990, Weber et al. 1994). Later analytical models of the PSF of a pinhole were used to perform iterative reconstructions (Li et al. 1995, Smith et al. 1998). The validity of the analytical PSF estimate depends on the agreement between the ideal system model and physical system. However, any deviations from perfect pinhole geometry can be characterised (Beque et al. 2003) and corrected (Beque et al. 2005) using a simple three-point-source measurement.

An alternative approach is to measure the PSF for each voxel position using a point source. The system matrix will then contain information specific to the system geometry, such as the collimator penetration and scatter, as well as any system asymmetries, but will lack the effects of attenuation and scatter in the patient.

The storage of an uncompressed measured system matrix file requires a large amount of storage media (Furenlid et al. 2002, Miller et al. 2011). Additionally, the measurement of a PSF at every voxel position is time-

consuming, and the system matrix must be recalibrated for each isotope. The system matrix file size can be reduced by fitting a Gaussian function to the PSFs on individual detectors and storing just the fitting parameters (van der Have et al. 2008) instead of the PSF projections. The PSF projections can then be calculated on the basis of the Gaussian parameters when necessary during reconstruction. Faster calibration can be achieved by measuring a sparser system matrix. A more densely sampled system matrix can then be calculated by interpolating the Gaussian parameters (Miller et al. 2011).

## Monte Carlo-based pinhole reconstruction

The system matrix can also be calculated using the Monte Carlo method. Either the system matrix can be pre-calculated and accessed when needed (Aguiar et al. 2014) or a Monte Carlo simulator can be incorporated directly into the ML-EM algorithm (Floyd et al. 1986, Elschot et al. 2013). Monte Carlo-based ML-EM image reconstruction involves using a Monte Carlo program as a forward-projector to calculate the estimated projections from the current source estimate at every iteration. If the Monte Carlo simulator accurately estimates the count flux, the Monte Carlo method is inherently quantitative, and the accuracy of the total activity recovery depends on the compliance between the model and the measurement system. In contrast, conventional quantitative SPECT depends on explicit calibration of a source with a known activity; therefore, the quantitative accuracy of SPECT depends on external factors such as the dose calibrator accuracy.

The Monte Carlo procedure is a forward-projector by design and therefore cannot be used in the back-projector step. Hence, the back-projection must be performed using a projector that is more approximate than a Monte Carlo-based projector. The use of two different system matrices in the forward and backward projection steps is referred to as dual-matrix image reconstruction. Dual-matrix image reconstruction has been shown to reduce reconstruction times without significantly reducing the reconstruction accuracy as long as the forward-projector is accurate (Zeng et al. 1991, Kamphuis et al. 1998, Zeng et al. 2000). However, some components of the back-projector model are more important than others, e.g. modelling the position-dependent resolution, and care should be taken to include the most relevant effects in the back-projector (Zeng et al. 2000).

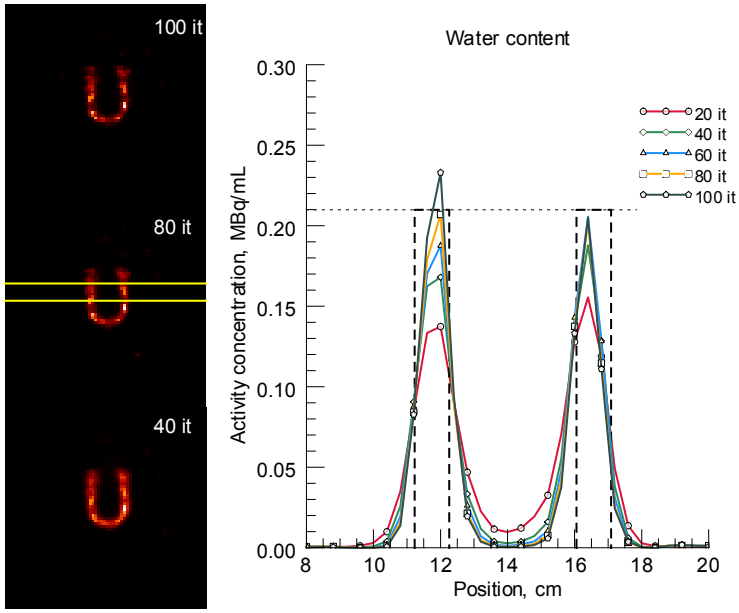


**Figure 21.** Profiles of a single slice of the myocardium generated using 20, 40, 60, 80, and 100 iterations. The projection data were measured using a $^{99}Tc^{m}$-filled cardiac phantom. The measurements were performed with a cardiac phantom mounted in a water-filled torso. The dotted line indicates the activity concentration defined by the phantom preparation, whereas the dashed lines indicate the myocardium wall positions. Using the Monte Carlo-based method, the correct myocardial wall activity concentration is recovered provided that a sufficient number of iterations are performed.

## Ray-tracing back-projector algorithm

Paper V describes the development and implementation of an approximate pinhole back-projector to enable Monte Carlo-based ML-EM reconstruction. Our back-projection method was modelled using a ray-tracing algorithm on a voxel-by-voxel basis.

For a given voxel, the irradiated detector bins are identified, and their respective fraction is determined by adapting a scalable grid. The algorithm can be summarised in three steps.

1. Determine the detector intercept point estimated by tracing a line from the centre of the current voxel through the centre of the pinhole. In practical terms, the reference system is first rotated twice according to polar and azimuthal angles specifying the detector position, thus aligning the $z$ axis of the reconstruction volume reference system with the pinhole axis. Subsequently, the detector

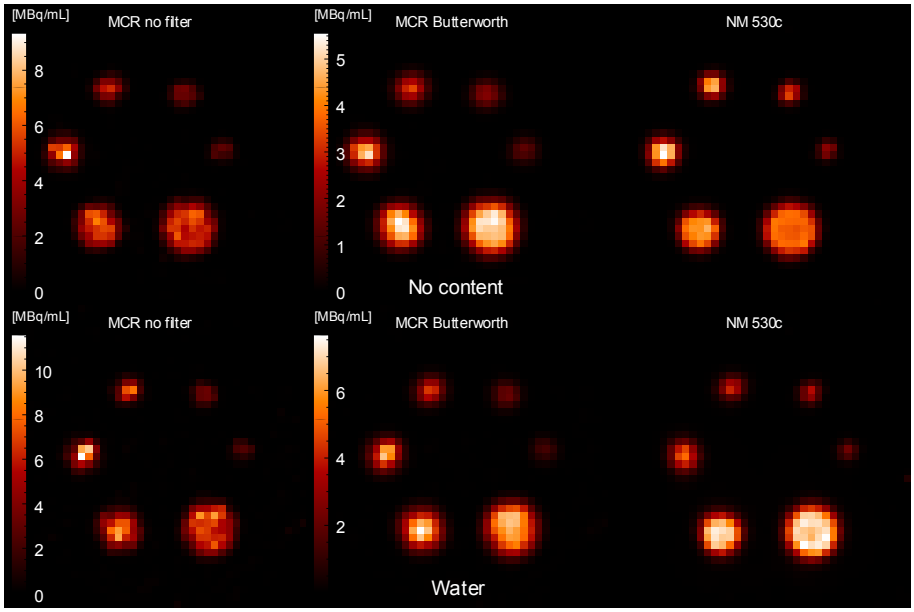


**Figure 22.** Qualitative comparison of the maximum-intensity projection images of the phantom data reconstructed using two different methods. The images in the left and centre column were reconstructed using the Monte Carlo-based ML-EM algorithm (MCR), while the clinical reconstructed images are on the right. The measurements were performed with a $^{99}Tc^{m}$-filled-sphere phantom with sphere volumes ranging from 0.5 mL to 16 mL. The spheres were mounted in a torso and measured while the torso was empty (upper) and filled with water (lower). MCR images in the centre column were filtered using a Butterworth filter (cut-off: 0.5, order: 2).

intercept point is given by scaling and mirroring the current voxel position by the magnification factor for the current detector–pinhole configuration.

2. Distribute the photons originating from within a single voxel over an area of the detector. This irradiated area is determined by the voxel size and a specific magnification factor for each reconstructed plane.

3. Model the spatially invariant efficiency by calculating a number of grid points proportional to the efficiency. The number of grid points is then distributed over the irradiated area. This procedure can be thought of as tracing several equally spaced lines from the central voxel plane through the pinhole centre.

The back-projected voxel value can then be calculated as the sum of the detector bin values (ratios) multiplied by a voxel-specific grid point factor. The grid point factor is determined by the number of grid points in the bin normalised to the total number of grid points in all of the bins. This process is then repeated for all of the voxels.

Despite the approximations introduced in the back-projection step, such as an infinitesimal pinhole size and no photon attenuation, the reconstruction produced quantitative images with acceptable image quality for phantom data. In figure 21, the profiles of the myocardial phantom walls illustrate that the method can recover the actual activity concentration in the myocardium. Again, this reconstruction was performed without any explicit calibration of the detector system.

A more qualitative comparison with the clinical reconstruction algorithm results is provided in figure 22. The spheres reconstructed using the clinical method (label: NM 530c) are more uniform, probably owing to the noise regularisation applied during the reconstruction (Green 1990), but they are similar in shape otherwise. Smoothing with a Butterworth filter can improve the noise characteristics of the Monte Carlo-based reconstruction images. For the largest sphere, a ringing artefact is visible in the NM 530c reconstruction results but not in those of the Monte Carlo-based reconstruction. In the Monte Carlo-based reconstruction results, the relative sphere intensity in the water-filled torso is similar to that in an empty torso since photon attenuation is included in the forward-projector model. In contrast, the absence of attenuation compensation in the NM 530c reconstruction method leads to non-homogeneous suppression of the sphere intensity when the torso is filled with water.

The conclusions of Paper V were that the combination of a Monte Carlo-based forward-projector and an analytical ray-tracing back-projector produces quantitative images with acceptable image quality and that no explicit calibration is necessary since the forward-projector model maintains a relationship between the count and the activity.

# Myocardial Perfusion Imaging

'Why don't you just set */fa:*11?'

**Michael Ljungberg when discussing measurements**

Myocardial ischemia is caused by coronary stenosis, i.e. abnormal narrowing of the coronary arteries, which supply the myocardium with blood. The location and degree of stenosis determine the extent and severity of the ischemic region. An ischemic region may recover if normal perfusion is restored and reperfusion can be performed pharmacologically or by using invasive methods such as percutaneous coronary intervention or coronary artery bypass surgery. If a region remains unperfused for an extended period of time, permanent loss of contractile function could occur (Soneson 2012). During exercise, the energy demand on the heart can be 4–6 times that when the heart is at rest. Therefore, myocardial ischemia sometimes manifests itself when the heart is stressed by physical or drug-induced exercise. This type of ischemia is called stress-induced ischemia.

Myocardial perfusion SPECT is an important non-invasive tool for diagnosing myocardial ischemia (Yoshinaga et al. 2011). This technique is used for risk stratification (Berman et al. 1995) and as a prognostic indicator (Iskander et al. 1998). Prognostic power studies have shown that this method has a high specificity, meaning that a patient with normal myocardial perfusion, based on the SPECT examination, has a low yearly average event rate and can therefore be excluded as a candidate for further investigation and treatment.

Typically, two SPECT studies are performed, each following one of two separate injections with the heart under stress or at rest. If the two SPECT studies are performed on the same day, the method is referred to as a one-day protocol, and if they are performed on separate days, it is called a two-day protocol. Two different isotopes are primarily used: $^{99}Tc^{m}$ (most commonly labelled Sestamibi™ or Tetrafosmin™) and $^{201}Tl$ (as Tl-chloride), and the radiopharmaceutical that is used depends on a variety of factors such as the desired patient throughput, dose limitations, and image-quality factors. If normal perfusion is recorded in the stress study, the rest study

can be omitted, thereby saving the patient from unnecessary radiation exposure (Gowd et al. 2014).

Initial studies of NM 530c showed that the acquisition times (Esteves et al. 2009) and patient absorbed doses could be decreased while maintaining the image quality of a conventional SPECT (Herzog et al. 2010, Oddstig et al. 2013). A thorough review of the clinical impacts of CZT-based myocardial perfusion SPECT imaging systems was provided by Ben-Haim et al. (2016). In short, the new systems have shown high agreement rates compared with those of conventional SPECT systems when diagnosing abnormal myocardial perfusion. Furthermore, the new systems can accurately detect patients with significant coronary obstructions, and the first studies on prognostic values have demonstrated that these values are well-correlated with those obtained using conventional SPECT systems.

A consistent feature in articles relating to the clinical introduction of semiconductor-based systems is the use of the newfound efficiency increase to increase patient throughput and/or lower patient doses. This alternative is both financially attractive and complies with the ALARA[5] principle (ICRP 2007). An alternative approach would be to increase the diagnostic value of an NM 530c study by using pinholes with smaller apertures, thereby enabling the system to resolve smaller variations in the activity distributions and potentially increasing the contrast. Paper VI describes the investigation of this hypothesis by using a realistic hybrid phantom to emulate a beating heart with a single lesion. Several phantom sets with varying lesion sizes and radiopharmaceutical uptake were generated, and projections were simulated using SIMIND and reconstructed using the reconstruction program described in Paper V. The simulated projections were scaled according to the acquisition time and administered an activity equal to that of the conventional SPECT protocol. The results of Paper VI suggest that decreasing the aperture size, instead of lowering patient absorbed doses and imaging time, does not lead to an increase in CNR. An observed increase in contrast for small lesions with smaller apertures is accompanied by an equal relative increase in noise. Recovered lesion contrast was highest for lesions with full transmurality and this group was stratified relative lesions with lower transmurality. This suggest that the ability to detect a lesion is more sensitive to changes in transmurality than to changes lesion extent.

[5] As Low As Reasonably Achievable.

# Summaries of Papers

**Paper I**

The imaging of pharmaceutical distributions in small animals is an important research tool for studying human diseases. Small animal SPECT imaging is a method of observing the biological processes of radio-labelled pharmaceuticals *in vivo*. In Paper I, we describe the determination of the reconstructed resolution for a prototype setup with a video-based detector system. A hot rod phantom filled with either $^{201}$Tl or $^{99}$Tc$^{m}$ was imaged with a single 1-mm pinhole and a video-based detector. The diameter of the smallest rods that could be separated in the reconstructed slices was 1.3 mm (the same as the distance between rod centres) for both isotopes.

**Paper II**

The ability to increase both the resolution and efficiency at the expense of a smaller FOV with pinhole collimation enables the use of a wide array of pinhole–detector combinations and designs for small-animal SPECT. Ideally, a material used for shielding and pinhole housing is cheap and has a high density and atomic number. In Paper II, we present a method of manufacturing pinhole geometries using an alloy called Rose's metal, which melts at 100 °C and does not contract when solidifying, implying that it can be cast into nearly any shape. Solid Rose's metal can be worked with a high precision and is not as soft as lead, for example. We successfully manufactured a detector-shielding pinhole housing and subsequently cast platinum pinholes into a Rose's metal insert.

**Paper III**

The small pinhole apertures used in pre-clinical SPECT imaging benefit from maximising the atomic number and density of the pinhole material. However, the materials used, e.g. gold and platinum, are typically expensive. An inexpensive alternative is Rose's metal. Compared to the aforementioned materials, Rose's metal has a low density and atomic number, which will affect the image quality negatively. In Paper III, we discuss the use of the simulation tool SIMIND to evaluate the pinhole capabilities of Rose's metal. Each material was evaluated in terms of its penetration- and scatter-to-total ratios, sensitivity, and resolution for different pinhole apertures and materials, incident angles, and photon energies. For the

imaging of low-energy emitters, e.g. $^{125}$I, the materials are equivalent. For $^{99}$Tc$^{m}$ and its 140 keV emission, the extra penetration and scatter associated with Rose's metal degrade the image quality but do not always do so substantially. Thus, Rose's metal can be used when the cost and design flexibility are important.

**Paper IV**

Myocardial perfusion imaging can be performed with dedicated camera systems. One such system is the GE Discovery NM 530c system, which is based on pinhole collimation and solid-state photon detection using CZT detectors. Compared to conventional scintillation detection, CZT is different in a number of aspects, e.g. the direct sensing of the generated charge offers a superior energy resolution but with a spectral redistribution of events due to electron-hole transport effects in the material. Paper IV describes the validation of a SIMIND simulation program that incorporates a charge collection model. The results of simulations and measurements were compared in terms of the energy spectra of several isotopes and the resolution and sensitivity of the projections for a point source. The paper concludes that it is feasible to simulate the GE Discovery NM 530c system using SIMIND.

**Paper V**

The accuracy of iterative image reconstruction results depends on how well the imaging system is modelled. The most accurate model of the image formation processes involves simulating a large number of photon histories using a Monte Carlo program, e.g. SIMIND. Paper V discusses the incorporation of SIMIND as a forward-projector in ML-EM reconstruction and its combination with a back-projector based on a ray-tracing algorithm. Projections acquired with the NM 530c were reconstructed, and the total activities in spheres of different sizes and the correct activity concentrations in a myocardial phantom could be recovered using our algorithm. Since SIMIND maintains a relationship between the number of detector counts and the source activity, no external calibration factor is necessary to achieve quantitative images.

**Paper VI**

Dedicated cardiac SPECT systems such as GE Discovery NM 530c can perform acquisition rapidly with low administered doses while maintaining the image quality achievable in conventional SPECT. An increased system sensitivity is generally not traded for an improved image quality but lowers the cost by increasing the patient throughput and reducing the radiation-induced risk by decreasing the administered activities. In theory, a smaller aperture improves the planar resolution and may increase the ability to detect smaller perfusion lesions in reconstructed images. In Paper VI, we describe an investigation of the potential improvements achievable in perfusion lesion recovery by generating a population of voxel-based phantoms with varying cardiac lesion sizes. Both projection simulation and reconstruction were

performed using SIMIND with the methods discussed in Papers III, IV and V. The results of Paper VI suggest that decreasing the aperture size, instead of lowering patient absorbed doses and imaging time, does not lead to an increase in CNR since any increase in contrast is accompanied by an equal increase in noise. Recovered lesion contrast was highest for lesions with full transmurality and this group was stratified relative lesions with lower transmurality. This suggest that the ability to detect a lesion is more sensitive to changes in transmurality than to changes lesion extent.

# Topics of Future Research

- Simulations of adaptive SPECT imaging systems, where the pinhole and detectors are moveable and thus able to perform serial acquisitions with varying spatial resolutions, efficiencies, and FOVs. The technique enables fast acquisition of a low-resolution overview scan with a subsequent focused high-resolution acquisition scan in the volume of interest.
- Include PSF modelling in the pinhole back-projector.
- Validation of SIMIND ML-EM for imaging $^{123}$I and $^{201}$Tl and the development of dual isotope reconstruction, e.g. $^{99}$Tc$^{m}$/$^{201}$Tl.

# Acknowledgement

> 'No one has studied the psychology of a dying party. It may be raging, howling, boiling, and then a fever sets in and a little silence and then quickly quickly it is gone, the guests go home or go to sleep or wander away to some other affair and they leave a dead body'.
>
> **John Steinbeck, Cannery Row**

There are many people who deserve my gratitude. Some, but not all, will be mentioned here.

- First and foremost, I would like to thank my supervisors. Michael, thank you for your willingness to 'adopt' me halfway through the Ph.D. when I returned from my clinical duties. I have truly enjoyed working with you, and you never cease to amaze me with your commitment to your work. I have especially enjoyed the 24/7 SIMIND customer service. Sven-Erik, your faith in me was always appreciated, and your never-ending enthusiasm was the driving force of the InSPECT project. I would also like to thank Kaj Ljunggren for his advice on detectors and for introducing me to C programming.
- I would like to thank all of my co-authors. Specifically, thanks to Johan Gustafsson for your pedagogical determination and perseverance, especially when faced with such worthy adversaries as my ignorance and short attention span.
- Thanks to Brian Miller at the Center for Gamma Ray Imaging at the University of Arizona in Tucson for providing me with the Bazooka hardware and software. Thank you also for inviting me into your home during my trips to Tucson.
- It is also a privilege to have had ready access to such high-quality craftsmanship as that provided by the oncology department workshop. Because of the friendly atmosphere, my visits were always longer than I first intended. Special thanks to Lars for your help with, primarily, InSPECT.

- I would also like to thank Jonathan Siikanen and Gustav Brolin, with whom I share(d) office space. Jonathan, my Guapa, I hope you get back to Skåne soon! Gustav, thanks for your wise counselling on nearly everything. Also, thanks to Erik Larsson for sharing your wisdom regarding bikes and for fixing coffee in the mornings.
- Thanks to the Ph.D. students and my colleagues at MSF for all of the fun times we had together. Also, my co-workers at Strålningsfysik, I really look forward to working with you all again. Thank you Jenny Oddstig for pushing me to resume my Ph.D. studies. Thank you Tomas Ohlsson for being supportive.
- I also greatly appreciate the times spent together with my Rocket League crew: Bryngylf, stepp0, and Coach Taylor.
- Thanks to Elias Kristensson for both your personal and professional advice. You are a true inspiration.
- I would like to thank my family and friends for your unwavering support through the years, which helped shape me into the person I am today.
- To my beloved Kristina, you mean so much to me and I am so glad that I get to finish this journey together with you.

# References


Abe, T. and S. Thurner (2005). "*Anomalous diffusion in view of Einstein's 1905 theory of Brownian motion.*" Physica A: Statistical Mechanics and its Applications **356**(2-4): 403-407.

Accorsi, R. and S. D. Metzler (2004). "*Analytic determination of the resolution-equivalent effective diameter of a pinhole collimator.*" IEEE Trans Med Imaging **23**(6): 750-763.

Aguiar, P., F. Pino, J. Silva-Rodriguez, J. Pavia, D. Ros, A. Ruibal and Z. El Bitar (2014). "*Analytical, experimental, and Monte Carlo system response matrix for pinhole SPECT reconstruction.*" Med Phys **41**(3): 032501.

Anger, H. O. (1952). "*Use of a gamma-ray pinhole camera for in vivo studies.*" Nature **170**(4318): 200-201.

Anger, H. O. (1958). "*Scintillation Camera.*" Review of Scientific Instruments **29**(1): 27-33.

Anger, H. O. (1967). "*Radioisotope Camera".* Instrumentation in Nuclear Medicine. G. J. Hine, Academic Press**:** 485-552.

Barrett, H. and W. J. Hunter (2005). "*Detectors for Small-Animal SPECT I".* Small-Animal Spect Imaging. M. Kupinski and H. Barrett, Springer US**:** 9-48.

Barrett, H. H., J. D. Eskin and H. B. Barber (1995). "*Charge Transport in Arrays of Semiconductor Gamma-Ray Detectors.*" Physical Review Letters **75**(1): 156-159.

Barrett, H. H. and W. C. J. Hunter (2005). "*Detectors for Small-Animal SPECT I".* Small-Animal Spect Imaging. M. A. Kupinski and H. H. Barrett, Springer US**:** 9-48.

Barrett, H. H. and K. J. Myers (2004). "*Foundations of image science*". Hoboken, NJ, Wiley-Interscience.

Barrett, H. H., D. W. Wilson and B. M. Tsui (1994). "*Noise properties of the EM algorithm: I. Theory.*" Phys Med Biol **39**(5): 833-846.

Beekman, F. and F. van der Have (2007). "*The pinhole: gateway to ultra-high-resolution three-dimensional radionuclide imaging.*" Eur J Nucl Med Mol Imaging **34**(2): 151-161.

Beekman, F. J., H. W. de Jong and S. van Geloven (2002). "*Efficient fully 3-D iterative SPECT reconstruction with Monte Carlo-based scatter compensation.*" IEEE Trans Med Imaging **21**(8): 867-877.

Beekman, F. J. and G. A. de Vree (2005). "*Photon-counting versus an integrating CCD-based gamma camera: important consequences for spatial resolution.*" Phys Med Biol **50**(12): N109-119.

Beekman, F. J., C. Kamphuis and E. C. Frey (1997). "*Scatter compensation methods in 3D iterative SPECT reconstruction: a simulation study.*" Phys Med Biol **42**(8): 1619-1632.

Beekman, F. J., C. Kamphuis and M. A. Viergever (1996). "*Improved SPECT quantitation using fully three-dimensional iterative spatially variant scatter response compensation.*" IEEE Trans Med Imaging **15**(4): 491-499.

Ben-Haim, S., J. Kennedy and Z. Keidar (2016). "*Novel Cadmium Zinc Telluride Devices for Myocardial Perfusion Imaging-Technological Aspects and Clinical Applications.*" Semin Nucl Med **46**(4): 273-285.

Beque, D., J. Nuyts, G. Bormans, P. Suetens and P. Dupont (2003). "*Characterization of pinhole SPECT acquisition geometry.*" IEEE Trans Med Imaging **22**(5): 599-612.

Beque, D., J. Nuyts, P. Suetens and G. Bormans (2005). "*Optimization of geometrical calibration in pinhole SPECT.*" IEEE Trans Med Imaging **24**(2): 180-190.

Berman, D. S., R. Hachamovitch, H. Kiat, I. Cohen, J. A. Cabico, F. P. Wang, J. D. Friedman, G. Germano, K. Van Train and G. A. Diamond (1995). "*Incremental value of prognostic testing in patients with known or suspected ischemic heart disease: a basis for optimal utilization of exercise technetium-99m sestamibi myocardial perfusion single-photon emission computed tomography.*" J Am Coll Cardiol **26**(3): 639-647.

Bocher, M., I. M. Blevis, L. Tsukerman, Y. Shrem, G. Kovalski and L. Volokh (2010). "*A fast cardiac gamma camera with dynamic SPECT capabilities: design, system validation and future potential.*" Eur J Nucl Med Mol Imaging **37**(10): 1887-1902.

Brolin, G., K. S. Gleisner and M. Ljungberg (2013). "*Dynamic (99m)Tc-MAG3 renography: images for quality control obtained by combining pharmacokinetic modelling, an anthropomorphic computer phantom and Monte Carlo simulated scintillation camera imaging.*" Phys Med Biol **58**(10): 3145-3161.

Brolin, G., J. Gustafsson, M. Ljungberg and K. S. Gleisner (2015). "*Pharmacokinetic digital phantoms for accuracy assessment of image-based dosimetry in (177)Lu-DOTATATE peptide receptor radionuclide therapy.*" Phys Med Biol **60**(15): 6131-6149.

Chan, C., J. Dey, Y. Grobshtein, J. Wu, Y. H. Liu, R. Lampert, A. J. Sinusas and C. Liu (2016). "*The impact of system matrix dimension on small FOV SPECT reconstruction with truncated projections.*" Med Phys **43**(1): 213.

Chen, L. and Y. X. Wei (2008). "*Monte Carlo simulations of the SNM spectra for CZT and NaI spectrometers.*" Appl Radiat Isot **66**(8): 1146-1150.

Cherry, S. R., J. A. Sorenson and M. E. Phelps (2012). "*Appendix G - Convolution".* Physics in Nuclear Medicine (Fourth Edition). S. R. Cherry, J. A. Sorenson and M. E. Phelps. Philadelphia, W.B. Saunders**:** 489-492.

Cherry, S. R., J. A. Sorenson and M. E. Phelps (2012). "*Chapter 1 - What Is Nuclear Medicine?".* Physics in Nuclear Medicine (Fourth Edition). S. R. Cherry, J. A. Sorenson and M. E. Phelps. Philadelphia, W.B. Saunders**:** 195-208.

Cherry, S. R., J. A. Sorenson and M. E. Phelps (2012). "*Chapter 14 - The Gamma Camera: Performance Characteristics".* Physics in Nuclear Medicine (Fourth Edition). S. R. Cherry, J. A. Sorenson and M. E. Phelps. Philadelphia, W.B. Saunders**:** 209-231.

Cherry, S. R., J. A. Sorenson and M. E. Phelps (2012). "*Chapter 17 - Single Photon Emission Computed Tomography".* Physics in Nuclear Medicine (Fourth Edition). S. R. Cherry, J. A. Sorenson and M. E. Phelps. Philadelphia, W.B. Saunders**:** 195-208.

de Jong, H. W. A. M., E. T. P. Slijpen and F. J. Beekman (2001). "*Acceleration of Monte Carlo SPECT simulation using convolution-based forced detection.*" IEEE Transactions on Nuclear Science **48**(1): 58-64.

Deleye, S., R. Van Holen, J. Verhaeghe, S. Vandenberghe, S. Stroobants and S. Staelens (2013). "*Performance evaluation of small-animal multipinhole muSPECT scanners for mouse imaging.*" Eur J Nucl Med Mol Imaging **40**(5): 744-758.

Deprez, K., L. R. Pato, S. Vandenberghe and R. Van Holen (2013). "*Characterization of a SPECT pinhole collimator for optimal detector usage (the lofthole).*" Phys Med Biol **58**(4): 859-885.

Dewaraja, Y. K., K. F. Koral and J. A. Fessler (2010). "*Regularized reconstruction in quantitative SPECT using CT side information from hybrid imaging.*" Phys Med Biol **55**(9): 2523-2539.

Einstein, A. (1905). "*Über die von der molekularkinetischen Theorie der Wärme geforderte Bewegung von in ruhenden Flüssigkeiten suspendierten Teilchen.*" Annalen der Physik **322**(8): 549-560.

El-Ali, H. H., J. Palmer, M. Carlsson, L. Edenbrandt and M. Ljungberg (2005). "*Comparison of 1- and 2-day protocols for myocardial SPECT: a Monte Carlo study.*" Clin Physiol Funct Imaging **25**(4): 189-195.

Elschot, M., M. G. Lam, M. A. van den Bosch, M. A. Viergever and H. W. de Jong (2013). "*Quantitative Monte Carlo-based 90Y SPECT reconstruction.*" J Nucl Med **54**(9): 1557-1563.

Erlandsson, K., I. Buvat, P. H. Pretorius, B. A. Thomas and B. F. Hutton (2012). "*A review of partial volume correction techniques for emission tomography and their applications in neurology, cardiology and oncology.*" Phys Med Biol **57**(21): R119-R159.

Esteves, F. P., P. Raggi, R. D. Folks, Z. Keidar, J. W. Askew, S. Rispler, M. K. O'Connor, L. Verdes and E. V. Garcia (2009). "*Novel solid-state-detector dedicated cardiac camera for fast myocardial perfusion imaging: multicenter comparison with standard dual detector cameras.*" J Nucl Cardiol **16**(6): 927-934.

Floyd, C. E., Jr., R. J. Jaszczak, K. L. Greer and R. E. Coleman (1986). "*Inverse Monte Carlo as a unified reconstruction algorithm for ECT.*" J Nucl Med **27**(10): 1577-1585.

Forrer, F., R. Valkema, B. Bernard, N. U. Schramm, J. W. Hoppin, E. Rolleman, E. P. Krenning and M. de Jong (2006). "*In vivo radionuclide uptake quantification using a multi-pinhole SPECT system to predict renal function in small animals.*" Eur J Nucl Med Mol Imaging **33**(10): 1214-1217.

Freitas, J. E. and A. E. Freitas (1994). "*Thyroid and parathyroid imaging.*" Seminars in Nuclear Medicine **24**(3): 234-245.

Frey, E. C. and B. M. Tsui (1996). "*A new method for modeling the spatially-variant, object-dependent scatter response function in SPECT*". IEEE Nuclear Science Symposium.

Furenlid, L. R., D. W. Wilson, C. Yi-chun, K. Hyunki, P. J. Pictraski, M. J. Crawford and H. H. Barrett (2002). "*FastSPECT II: a second-generation high-resolution dynamic SPECT imager*". IEEE Nuclear Science Symposium Conference Record.

Gambhir, S. S., D. S. Berman, J. Ziffer, M. Nagler, M. Sandler, J. Patton, B. Hutton, T. Sharir, S. B. Haim and S. B. Haim (2009). "*A novel high-sensitivity rapid-acquisition single-photon cardiac imaging camera.*" J Nucl Med **50**(4): 635-643.

Goorden, M. C. and F. J. Beekman (2010). "*High-resolution tomography of positron emitters with clustered pinhole SPECT.*" Phys Med Biol **55**(5): 1265-1277.

Goorden, M. C., F. van der Have, R. Kreuger, R. M. Ramakers, B. Vastenhouw, J. P. Burbach, J. Booij, C. F. Molthoff and F. J. Beekman (2013). "*VECTor: a preclinical imaging system for simultaneous submillimeter SPECT and PET.*" J Nucl Med **54**(2): 306-312.

Gowd, B. M., G. V. Heller and M. W. Parker (2014). "*Stress-only SPECT myocardial perfusion imaging: a review.*" J Nucl Cardiol **21**(6): 1200-1212.

Green, P. J. (1990). "*Bayesian reconstructions from emission tomography data using a modified EM algorithm.*" IEEE Trans Med Imaging **9**(1): 84-93.

Gros d'Aillon, E., J. Tabary, A. Glière and L. Verger (2006). "*Charge sharing on monolithic CdZnTe gamma-ray detectors: A simulation study.*" Nuclear Instruments and Methods in Physics Research Section A: Accelerators, Spectrometers, Detectors and Associated Equipment **563**(1): 124-127.

Guerra, P., A. Santos and D. G. Darambara (2008). "*Development of a simplified simulation model for performance characterization of a pixellated CdZnTe multimodality imaging system.*" Phys Med Biol **53**(4): 1099-1113.

Gustafsson, J., G. Brolin, M. Cox, M. Ljungberg, L. Johansson and K. Sjögreen-Gleisner (2015). "*Uncertainty propagation for SPECT/CT-based renal dosimetry in 177 Lu peptide receptor radionuclide therapy.*" Phys Med Biol **60**(21): 8329.

Harrison, R. "*SimSET Home Page.*" Retrieved 207-05-22, from http://depts.washington.edu/simset/html/simset_main.html.

Haynor, D. R. and R. L. Harrison (2013). "*Variance reduction techniques*", CRC Press.

Hebert, T. and R. Leahy (1989). "*A generalized EM algorithm for 3-D Bayesian reconstruction from Poisson data using Gibbs priors.*" IEEE Trans Med Imaging **8**(2): 194-202.

Hebert, T. J. (1990). "*Statistical Stopping Criteria for Iterative Maximum-Likelihood Reconstruction of Emission Images.*" Phys Med Biol **35**(9): 1221-1232.

Hecht, K. (1932). "*Zum Mechanismus des lichtelektrischen Primärstromes in isolierenden Kristallen.*" Zeitschrift für Physik **77**(3): 235-245.

Herzog, B. A., R. R. Buechel, R. Katz, M. Brueckner, L. Husmann, I. A. Burger, A. P. Pazhenkottil, I. Valenta, O. Gaemperli, V. Treyer and P. A. Kaufmann (2010). "*Nuclear myocardial perfusion imaging with a cadmium-zinc-telluride detector technique: optimized protocol for scan time reduction.*" J Nucl Med **51**(1): 46-51.

Hindorf, C., J. Oddstig, F. Hedeer, M. J. Hansson, J. Jogi and H. Engblom (2014). "*Importance of correct patient positioning in myocardial perfusion SPECT when using a CZT camera.*" J Nucl Cardiol **21**(4): 695-702.

Hudson, H. M. and R. S. Larkin (1994). "*Accelerated image reconstruction using ordered subsets of projection data.*" IEEE Trans Med Imaging **13**(4): 601-609.

Hurley, P. J., H. W. Strauss, P. Pavoni, J. K. Langan and H. N. Wagner (1971). "*The Scintillation Camera with Pinhole Collimator in Thyroid Imaging.*" Radiology **101**(1): 133-138.

Hutton, B. F. (2011). "*Recent advances in iterative reconstruction for clinical SPECT/PET and CT.*" Acta Oncol **50**(6): 851-858.

Hutton, B. F., I. Buvat and F. J. Beekman (2011). "*Review and current status of SPECT scatter correction.*" Phys Med Biol **56**(14): R85-112.

ICRP (2007). "*ICRP Publication 105. Radiation protection in medicine.*" Ann ICRP **37**(6): 1-63.

Iskander, S. and A. E. Iskandrian (1998). "*Risk assessment using single-photon emission computed tomographic technetium-99m sestamibi imaging.*" J Am Coll Cardiol **32**(1): 57-62.

Jan, S., G. Santin, D. Strul, S. Staelens, K. Assie, D. Autret, S. Avner, R. Barbier, M. Bardies, P. M. Bloomfield, D. Brasse, V. Breton, P. Bruyndonckx, I. Buvat, A. F. Chatziioannou, Y. Choi, Y. H. Chung, C. Comtat, D. Donnarieix, L. Ferrer, S. J. Glick, C. J. Groiselle, D. Guez, P. F. Honore, S. Kerhoas-Cavata, A. S. Kirov, V. Kohli, M. Koole, M. Krieguer, D. J. van der Laan, F. Lamare, G. Largeron, C. Lartizien, D. Lazaro, M. C. Maas, L. Maigne, F. Mayet, F. Melot, C. Merheb, E. Pennacchio, J. Perez, U. Pietrzyk, F. R. Rannou, M. Rey, D. R. Schaart, C. R. Schmidtlein, L. Simon, T. Y. Song, J. M. Vieira, D. Visvikis, R. Van de Walle, E. Wieers and C. Morel (2004). "*GATE: a simulation toolkit for PET and SPECT.*" Phys Med Biol **49**(19): 4543-4561.

Jaszczak, R. J., K. L. Greer, C. E. Floyd, Jr., C. C. Harris and R. E. Coleman (1984). "*Improved SPECT quantification using compensation for scattered photons.*" J Nucl Med **25**(8): 893-900.

Jaszczak, R. J., J. Li, H. Wang, M. R. Zalutsky and R. E. Coleman (1994). "*Pinhole collimation for ultra-high-resolution, small-field-of-view SPECT.*" Phys Med Biol **39**(3): 425-437.

Jerram, P., P. J. Pool, R. Bell, D. J. Burt, S. Bowring, S. Spencer, M. Hazelwood, I. Moody, N. Catlett and P. S. Heyes (2001). "*The LLCCD: low-light imaging without the need for an intensifier*". SPIE, Sensors and Camera Systems for Scientific, Industrial, and Digital Photography Applications II.

Kahn, H. (1956). "*Applications of Monte Carlo*". Santa Monica.

Kamphuis, C., F. J. Beekman, P. P. van Rijk and M. A. Viergever (1998). "*Dual matrix ordered subsets reconstruction for accelerated 3D scatter compensation in single-photon emission tomography.*" Eur J Nucl Med **25**(1): 8-18.

Kettle, A. G. and M. J. O'Doherty (2006). "*Parathyroid Imaging: How Good Is It and How Should It Be Done?*" Seminars in Nuclear Medicine **36**(3): 206-211.

King, M. A., D. J. deVries, T. S. Pan, P. H. Pretorius and J. A. Case (1997). "*An investigation of the filtering of TEW scatter estimates used to compensate for scatter with ordered subset reconstructions.*" IEEE Trans Nucl Sci **44**(3): 1140-1145.

Knoll, G. F. (2010). "*Radiation detection and measurement*", New York : Wiley, cop. 2010.

Koral, K. F. and Y. K. Dewaraja (2013). "*Monte Carlo in SPECT Scatter Correction*", CRC Press.

Lalush, D. S. and M. N. Wernick (2004). "*Iterative Image Reconstruction*". San Diego, Elsevier Academic Press.

Land, M. F. (2003). "*The spatial resolution of the pinhole eyes of giant clams (Tridacna maxima).*" Proc Biol Sci **270**(1511): 185-188.

Lange, K. and R. Carson (1984). "*EM reconstruction algorithms for emission and transmission tomography.*" J Comput Assist Tomogr **8**(2): 306-316.

Lazaro, D., Z. El Bitar, V. Breton, D. Hill and I. Buvat (2005). "*Fully 3D Monte Carlo reconstruction in SPECT: a feasibility study.*" Phys Med Biol **50**(16): 3739-3754.

Li, J., R. J. Jaszczak and R. E. Coleman (1995). "*Maximum likelihood reconstruction for pinhole SPECT with a displaced center-of-rotation.*" IEEE Trans Med Imaging **14**(2): 407-409.

Liu, S., M. A. King, A. B. Brill, M. G. Stabin and T. H. Farncombe (2008). "*Convolution-Based Forced Detection Monte Carlo Simulation Incorporating Septal Penetration Modeling.*" IEEE Trans Nucl Sci **55**(3): 967-974.

Ljungberg, M., M. A. King, G. J. Hademenos and S. E. Strand (1994). "*Comparison of four scatter correction methods using Monte Carlo simulated source distributions.*" J Nucl Med **35**(1): 143-151.

Ljungberg, M. and P. H. Pretorius (2017). "*SPECT/CT: an update on technological developments and clinical applications.*" Br J Radiol: 20160402.

Ljungberg, M. and S. E. Strand (1989). "*A Monte Carlo program for the simulation of scintillation camera characteristics.*" Comput Methods Programs Biomed **29**(4): 257-272.

Ljungberg, M. and S. E. Strand (1991). "*Attenuation and scatter correction in SPECT for sources in a nonhomogeneous object: a monte Carlo study.*" J Nucl Med **32**(6): 1278-1284.

Martinsson, E., C. Hindorf and J. Oddstig (2016). Evaluation of differences in attenuation pattern for myocardial perfusion scintigraphy between CZT and conventional gamma cameras. Lund University Libraries, Lund University.

Meikle, S. R., P. Kench, M. Kassiou and R. B. Banati (2005). "*Small animal SPECT and its place in the matrix of molecular imaging technologies.*" Phys Med Biol **50**(22): R45-61.

Metzler, S. D., J. E. Bowsher, K. L. Greer and R. J. Jaszczak (2002). "*Analytic determination of the pinhole collimator's point-spread function and RMS resolution with penetration.*" IEEE Trans Med Imaging **21**(8): 878-887.

Metzler, S. D., J. E. Bowsher, M. F. Smith and R. J. Jaszczak (2001). "*Analytic determination of pinhole collimator sensitivity with penetration.*" IEEE Trans Med Imaging **20**(8): 730-741.

Miller, B. W., H. B. Barber, H. H. Barrett, Z. Liu, V. V. Nagarkar and L. R. Furenlid (2012). "*Progress in BazookaSPECT: High-Resolution, Dynamic Scintigraphy with Large-Area Imagers.*" Proc SPIE Int Soc Opt Eng **8508**.

Miller, B. W., H. H. Barrett, L. R. Furenlid, H. B. Barber and R. J. Hunter (2008). "*Recent advances in BazookaSPECT: Real-time data processing and the development of a gamma-ray microscope.*" Nucl Instrum Methods Phys Res A **591**(1): 272-275.

Miller, B. W., H. Bradford Barber, H. H. Barrett, D. W. Wilson and C. Liying (2006). "*A Low-Cost Approach to High-Resolution, Single-Photon Imaging Using Columnar Scintillators and Image Intensifiers*". Nuclear Science Symposium Conference Record.

Miller, B. W., L. R. Furenlid, S. K. Moore, H. Bradford Barber, V. V. Nagarkar and H. H. Barrett (2009). "*System integration of FastSPECT III, a dedicated SPECT rodent-brain imager based on BazookaSPECT detector technology*". IEEE Nuclear Science Symposium Conference Record.

Miller, B. W., J. W. Moore, M. E. Gehm, L. R. Furenlid and H. H. Barrett (2009). "*Novel Applications of Rapid Prototyping in Gamma-ray and X-ray Imaging.*" IEEE Nucl Sci Symp Conf Rec (1997) **2009**: 3322-3326.

Miller, B. W., R. Van Holen, H. H. Barrett and L. R. Furenlid (2011). "*A system calibration and fast iterative reconstruction method for next-generation SPECT imagers*". IEEE Nucl Sci Symp Conf Rec, Valencia.

Oddstig, J., F. Hedeer, J. Jogi, M. Carlsson, C. Hindorf and H. Engblom (2013). "*Reduced administered activity, reduced acquisition time, and preserved image quality for the new CZT camera.*" J Nucl Cardiol **20**(1): 38-44.

Ogawa, K. (1994). "*Simulation study of triple-energy-window scatter correction in combined Tl-201, Tc-99m SPECT.*" Ann Nucl Med **8**(4): 277-281.

Ouyang, J., G. El Fakhri and S. C. Moore (2007). "*Fast Monte Carlo based joint iterative reconstruction for simultaneous 99mTc/ 123I SPECT imaging.*" Med Phys **34**(8): 3263-3272.

Paix, D. (1967). "*Pinhole imaging of gamma rays.*" Physics in Medicine and Biology **12**(4): 489.

Palmer, J. and P. Wollmer (1990). "*Pinhole emission computed tomography: method and experimental evaluation.*" Phys Med Biol **35**(3): 339-350.

Patton, J. A. and T. G. Turkington (2008). "*SPECT/CT physical principles and attenuation correction.*" J Nucl Med Technol **36**(1): 1-10.

Peterson, M., K. Ljunggren, L. Andersson-Ljus, B. Miller and S. E. Strand (2010). "*A method for using high density fusible Rose's metal with high precision machining in small animal imaging applications*". Nuclear Science Symposium Conference Record (NSS/MIC), 2010 IEEE.

Peterson, M., S. E. Strand and M. Ljungberg (2015). "*Using Rose's metal alloy as a pinhole collimator material in preclinical small-animal imaging: a Monte Carlo evaluation.*" Med Phys **42**(4): 1698-1709.

Peterson, T. E. and L. R. Furenlid (2011). "*SPECT detectors: the Anger Camera and beyond.*" Physics in Medicine and Biology **56**(17): R145-182.

Peterson, T. E. and L. R. Furenlid (2011). "*SPECT detectors: the Anger Camera and beyond.*" Phys Med Biol **56**(17): R145-182.

Ramo, S. (1939). "*Currents Induced by Electron Motion.*" Proceedings of the IRE **27**(9): 584-585.

Rittenbach, A., J. Xu, A. M. El-Sharkawy, W. A. Edelstein, K. Parnham, J. Hugg and B. M. W. Tsui (2013). "*Continuing evaluation of an MR compatible SPECT insert for simultaneous SPECT-MR imaging of small animals*". IEEE Nuclear Science Symposium and Medical Imaging Conference.

Rogulski, M. M., H. B. Barber, H. H. Barrett, R. L. Shoemaker and J. M. Woolfenden (1993). "*Ultra-High-Resolution Brain Spect Imaging - Simulation Results.*" IEEE Trans Nucl Sci **40**(4): 1123-1129.

Rogulski, M. M., H. B. Barber, H. H. Barrett, R. L. Shoemaker and J. M. Woolfenden (1993). "*Ultra-high-resolution brain SPECT imaging: simulation results.*" Nuclear Science, IEEE Transactions on **40**(4): 1123-1129.

Roncali, E. and S. R. Cherry (2011). "*Application of silicon photomultipliers to positron emission tomography.*" Ann Biomed Eng **39**(4): 1358-1377.

Rowland, D. J. and S. R. Cherry (2008). "*Small-animal preclinical nuclear medicine instrumentation and methodology.*" Semin Nucl Med **38**(3): 209-222.

Salvat, F., J. M. Fernández-Varea and J. Sempau. (2014). "*PENELOPE2014: A Code System for Monte-Carlo Simulation of Electron and Photon Transport.*" from https://www.oecd-nea.org/tools/abstract/detail/nea-1525.

Schramm, N. U., G. Ebel, U. Engeland, T. Schurrat, M. Behe and T. M. Behr (2003). "*High-resolution SPECT using multipinhole collimation.*" IEEE Trans Nucl Sci **50**(3): 315-320.

Segars, W. P., G. Sturgeon, S. Mendonca, J. Grimes and B. M. Tsui (2010). "*4D XCAT phantom for multimodality imaging research.*" Med Phys **37**(9): 4902-4915.

Shepp, L. A. and Y. Vardi (1982). "*Maximum likelihood reconstruction for emission tomography.*" IEEE Trans Med Imaging **1**(2): 113-122.

Shockley, W. (1938). "*Currents to Conductors Induced by a Moving Point Charge.*" Journal of Applied Physics **9**(10): 635-636.

Smith, M. F. and R. J. Jaszczak (1997). "*The effect of gamma ray penetration on angle-dependent sensitivity for pinhole collimation in nuclear medicine.*" Med Phys **24**(11): 1701-1709.

Smith, M. F. and R. J. Jaszczak (1998). "*An analytic model of pinhole aperture penetration for 3D pinhole SPECT image reconstruction.*" Phys Med Biol **43**(4): 761.

Snyder, W. S., M. R. Ford and G. G. Warner (1978). Estimates of Specific Absorbed Fraction for Photon Sources Uniformly Distributed in Various Organs of a Heterogeneous Phantom. New York, Society of Nuclear Medicine.

Soneson, H. (2012). "*Methods for quantitative analysis of myocardial perfusion SPECT : validated with magnetic resonance imaging, phantom studies and expert readers*". PhD, Lund university.

Suzuki, K., I. Horiba and N. Sugie (2000). "*Fast connected-component labeling based on sequential local operations in the course of forward raster scan followed by backward raster scan*". Proceedings 15th International Conference on Pattern Recognition.

Timmins, R., T. D. Ruddy and R. G. Wells (2015). "*Patient position alters attenuation effects in multipinhole cardiac SPECT.*" Med Phys **42**(3): 1233-1240.

Tsui, B. M., E. C. Frey, X. Zhao, D. S. Lalush, R. E. Johnston and W. H. McCartney (1994). "*The importance and implementation of accurate 3D compensation methods for quantitative SPECT.*" Phys Med Biol **39**(3): 509-530.

van Audenhaege, K., R. van Holen, S. Vandenberghe, C. Vanhove, S. D. Metzler and S. C. Moore (2015). "*Review of SPECT collimator selection, optimization, and fabrication for clinical and preclinical imaging.*" Med Phys **42**(8): 4796-4813.

Van Audenhaege, K., C. Vanhove, S. Vandenberghe and R. Van Holen (2015). "*The evaluation of data completeness and image quality in multiplexing multi-pinhole SPECT.*" IEEE Trans Med Imaging **34**(2): 474-486.

van der Have, F. and F. J. Beekman (2004). "*Photon penetration and scatter in micro-pinhole imaging: a Monte Carlo investigation.*" Phys Med Biol **49**(8): 1369-1386.

van der Have, F. and F. J. Beekman (2006). "*Penetration, Scatter and Sensitivity in Channel Micro-Pinholes for SPECT: A Monte Carlo Investigation.*" Nuclear Science, IEEE Transactions on **53**(5): 2635-2645.

van der Have, F. and F. J. Beekman (2006). "*Penetration, Scatter and Sensitivity in Channel Micro-Pinholes for SPECT: A Monte Carlo Investigation.*" IEEE Trans Nucl Sci **53**(5): 2635-2645.

van der Have, F., B. Vastenhouw, R. M. Ramakers, W. Branderhorst, J. O. Krah, C. Ji, S. G. Staelens and F. J. Beekman (2009). "*U-SPECT-II: An Ultra-High-Resolution Device for Molecular Small-Animal Imaging.*" J Nucl Med **50**(4): 599-605.

van der Have, F., B. Vastenhouw, M. Rentmeester and F. J. Beekman (2008). "*System calibration and statistical image reconstruction for ultra-high resolution stationary pinhole SPECT.*" IEEE Trans Med Imaging **27**(7): 960-971.

Vandenberghe, S. and P. K. Marsden (2015). "*PET-MRI: a review of challenges and solutions in the development of integrated multimodality imaging.*" Phys Med Biol **60**(4): R115.

Wangerin, K., Y. Du and F. Jansen (2011). "*CZT performance for different anode pixel geometries and data corrections.*" Nuclear Instruments and Methods in Physics Research Section A: Accelerators, Spectrometers, Detectors and Associated Equipment **648, Supplement 1**: S37-S41.

Weber, D. A., M. Ivanovic, D. Franceschi, S. E. Strand, K. Erlandsson, M. Franceschi, H. L. Atkins, J. A. Coderre, H. Susskind, T. Button and et al. (1994). "*Pinhole SPECT: an approach to in vivo high resolution SPECT imaging in small laboratory animals.*" J Nucl Med **35**(2): 342-348.

Wilderman, S. J. and Y. Namito (2013). "*The EGS Family of Code Systems*", CRC Press.

Yoshinaga, K., O. Manabe and N. Tamaki (2011). "*Physiological assessment of myocardial perfusion using nuclear cardiology would enhance coronary artery disease patient care: which imaging modality is best for evaluation of myocardial ischemia? (SPECT-side).*" Circ J **75**(3): 713-722; discussion 731.

Zeng, G. L. and G. T. Gullberg (2000). "*Unmatched projector/backprojector pairs in an iterative reconstruction algorithm.*" IEEE Trans Med Imaging **19**(5): 548-555.

Zeng, G. L., G. T. Gullberg, B. M. W. Tsui and J. A. Terry (1991). "*Three-dimensional iterative reconstruction algorithms with attenuation and geometric point response correction.*" IEEE Trans Nucl Sci **38**(2): 693-702.

Zubal, G. I. and P. W. Segars (2013). "*Anthropomorphic Phantoms: Early Development and Current Advances*", CRC Press.

Printed by Media-Tryck, Lund 2017 NORDIC ECOLABEL. 3041 0903

LUND
UNIVERSITY

Faculty of Science
Department of Medical Radiation Physics

ISBN 978-91-7753-377-1
ISBN 978-91-7753-378-8